

# **Examination of the Effect of TiN Particles and Grain Size on the Charpy Impact Transition Temperature in Steels**

by

**Jinlong Du**

A thesis submitted to the University of Birmingham

for the degree of MASTER OF RESEARCH

**School of Metallurgy and Materials**

**The University of Birmingham**

**Faculty of Engineering**

**December 2011**

**UNIVERSITY OF  
BIRMINGHAM**

**University of Birmingham Research Archive**

**e-theses repository**

This unpublished thesis/dissertation is copyright of the author and/or third parties. The intellectual property rights of the author or third parties in respect of this work are as defined by The Copyright Designs and Patents Act 1988 or as modified by any successor legislation.

Any use made of information contained in this thesis/dissertation must be in accordance with that legislation and must be properly acknowledged. Further distribution or reproduction in any format is prohibited without the permission of the copyright holder.

## Preface

This dissertation is submitted for the degree of Master of Research at the University of Birmingham. It describes research carried out in the School of Metallurgy and Materials, University of Birmingham, between October 2010 and September 2011, under the supervision of Professor C. L. Davis and Dr. M. Strangwood. Except where appropriately referenced, this work is entirely original, and contains nothing that is the outcome of collaboration. No part of this dissertation has been, or is concurrently being, submitted for any other degree, diploma or any other qualification. It does not exceed 15,000 words in length.

J. Du

November, 2011

## **Abstract**

The toughness of ferritic steels is influenced by the grain size distribution, second phase, precipitates and coarse inclusions. In this work an examination of the effect of coarse TiN particles ( $> 0.5 \mu\text{m}$ ) and ferrite grain size on the Charpy impact transition temperature in high strength low alloyed steels has been carried out. Steels with high (up to 0.045 wt %) Ti content, have been heat-treated and furnace cooled to obtain a ferrite-pearlite microstructure with different ferrite grain sizes. Coarse TiN particle size and ferrite grain size distributions have been measured and Charpy impact testing has been carried out. Scanning electron microscopy (SEM) analysis was used to measure the grain boundary carbide thickness and for fractographic analysis to determine if the coarse TiN particles are acting as cleavage initiation sites. The Charpy ductile-brittle transition temperatures (DBTT) have been predicted using standard literature equations, and compared to the measured values. It has been found that there was no significant effect of the coarse TiN particles on shifting the Charpy impact DBTT with the DBTT values being adequately predicted by literature equation across the ferrite grain size range from  $5 - 27 \mu\text{m}$ .

Key words: TiN, Grain size, Charpy impact test, DBTT, Steels

## Acknowledgement

I would like to thank my supervisors, Professor Claire Davis and Dr. Martin Strangwood, for their enthusiasm, support, advice, patience, encouragement, guidance and assistance through the course of this work.

Also my thanks must go to the staff in the School of Metallurgy and Materials, especially Mr. Michael Cunningham, for the help with mechanical testing, and Mr. Paul Stanley, for his help with electron microscopy. Particular thanks must go to Professor Paul Bowen, Professor Hanshan Dong, Professor Ian Jones, Dr. Yu Lung Chiu, Professor Tim Button and Dr. Andy Williams, for their help in academic teaching courses. I would like to thank my MRes tutors, Professor Nick Green and Ms Michelle Tuttle, for their guidance both in the early days and the following year of this project.

My special thanks are due to past and present Phase Transformation Group members, Dr. Carl Slater, Mr. Xi Liu, Mr. Lei Zhou, Mr. John-Paul Tovee, Mr. George Roberts, Ms. Rachel Punch and Mr. Guowei Zhang, their support and help are much appreciated.

# Contents

1	Introduction.....	1
2	Literature Review.....	3
2.1	Titanium in Steels .....	3
2.2	Titanium Nitride Particles .....	4
2.2.1	TiN Particle Characteristics .....	4
2.2.2	Solubility and Composition of TiN .....	5
2.3	Effect of Grain Size on Mechanical Properties in Steels.....	7
2.4	Micromechanics for Cleavage Fracture.....	7
2.5	Micro-crack initiated from TiN particles .....	9
2.6	Critical processes in TiN particle initiated cleavage fracture.....	11
2.7	Ductile-brittle transition temperature (DBTT).....	12
2.8	Predictions of DBTT .....	13
2.8	Overall summary of steel toughness affected by coarse TiN particles.....	14
3	Experimental Methods.....	21
3.1	Materials.....	21
3.2	Heat Treatment Methods.....	22
3.2	Metallography and image analysis .....	22
3.3	Scanning electron microscopy .....	23
3.4	Hardness tests and yield strength values.....	24

*Contents*

3.6 Charpy impact tests.....	24
4 Results .....	26
4.1 Optical microstructure.....	26
4.2 TiN particle investigation.....	27
4.3 Hardness and Strength.....	28
4.4 Grain Boundary Carbide Thickness .....	29
4.5 DBTT Values .....	30
4.6 Fracture Surface Analysis.....	31
5 Discussion .....	49
5.1 Crack Nucleation .....	49
5.2 Combination of the Effect of Particles and Grain Size.....	52
5.3 Relationship between TiN particles, grain size and impact toughness.....	54
6 Conclusions and Future Work.....	59
6.1 Conclusions .....	59
6.2 Suggestions for future work.....	60
References .....	61

# List of Tables

TABLE 2.1. LITERATURE DATA ON THE ROLE OF TiN ON FRACTURE IN STEELS .....	15
TABLE 3.1 COMPOSITIONS OF STEELS INVESTIGATED (WT %).....	21
TABLE 4.1. GRAIN SIZE AND PEARLITE AMOUNT FOR THE DIFFERENT SAMPLES .....	26
TABLE 4.2. COARSE TiN PARTICLE SIZE AND NUMBER DENSITY IN THE INVESTIGATED STEELS .....	28
TABLE 4.3. MACRO-HARDNESS ( $H_V$ ) VALUES AND PREDICTED YIELD STRENGTH OF THE HEAT TREATED SAMPLES .....	29
TABLE 4.4. GRAIN BOUNDARY CARBIDE THICKNESS ( $t$ ) OF THE STEELS INVESTIGATED (MM).....	29
TABLE 4.5. COMPARISON OF EXPERIMENTAL AND PREDICTED DBTT VALUES .....	30
TABLE 5.1. COMPARISON OF $\Sigma_{PM}$ AND $\Sigma_{MM}$ VALUES OF THREE STEELS .....	52

# List of Figures

FIGURE 2.1-FE-FE <sub>3</sub> C PHASE DIAGRAM <sup>10</sup> .....	16
FIGURE 2.2-EFFECT OF TITANIUM ON THE $\Gamma$ -PHASE FIELD <sup>10</sup> .....	17
FIGURE 2.3-EFFECT OF ALLOY ELEMENTS ON TTT CURVE OF STEEL: A) ORIGINAL TTT GRAPH AND B) EFFECT OF DIFFERENT ALLOY ELEMENTS <sup>20</sup> .....	18
FIGURE 2.4-SHAPE OF LARGE TiN INCLUSIONS UNDER AN OPTICAL MICROSCOPE, NOTE THAT Al <sub>2</sub> O <sub>3</sub> PARTICLES (DARK) CAN BE OBSERVED IN SOME TiN INCLUSIONS <sup>4</sup> .....	18
FIGURE 2.5-A) TESSELLATED STRESS DISTRIBUTIONS AROUND A TiN PARTICLE AND B) DISLOCATION PILE-UP AROUND A TiN PARTICLE TO INITIATE MICROCRACK <sup>24</sup> .....	19
FIGURE 2.6-VARIATION OF CLEAVAGE FRACTURE STRENGTHS AT DIFFERENT TEMPERATURES <sup>24</sup> ....	19
FIGURE 2.7-THE EFFECT OF TEMPERATURE ON THE CRITICAL CLEAVAGE FRACTURE STRESS AND CRITICAL RESOLVED SHEAR STRESS OF SINGLE CRYSTAL PURE IRON <sup>22</sup> .....	20
FIGURE 2.8-IMPACT TRANSITION CURVES FOR DIFFERENT MATERIALS <sup>22</sup> .....	20
FIGURE 3.1-HEAT TREATMENT METHODS A) FOR STEEL 1 AND 3, B) FOR STEEL 2 .....	25
FIGURE 3.2-STANDARD CHARPY V-NOTCH SPECIMENS .....	25
FIGURE 4.1-OPTICAL MICROGRAPH SHOWING THE FERRITE+PEARLITE MICROSTRUCTURE WITH DIFFERENT GRAIN SIZES OF INVESTIGATED STEELS AFTER AUSTENITISING AT DIFFERENT TEMPERATURES FOR 30 MINUTES: A) S1-900, B) S1-1100, C) S1-1200, D) S2-900, E) S2-1100, F) S3-1100 AND E) S3-1200.....	37
FIGURE 4.2-GRAIN SIZE DISTRIBUTIONS (IN NUMBER FREQUENCY AND AREA FRACTION) OF THE MATERIALS AFTER HEAT TREATMENTS. ....	38

*List of Figures*

FIGURE 4.3-A) A TYPICAL TiN (GREY) PARTICLE FOUND IN S1-1100 SURROUNDING AN Al <sub>2</sub> O <sub>3</sub> (BLACK) INCLUSION, B) EDS RESULT OF THE BLACK CENTRE OF PARTICLE AND C) EDS RESULT OF THE PARTICLE AWAY FROM THE BLACK CENTRE, THE Nb PEAK IS LIKELY TO BE FROM Nb(C,N) THAT PRECIPITATED ON THE TiN INCLUSION.....	39
FIGURE 4.4-GRAIN BOUNDARY CARBIDES FOUND IN THE HEAT TREATED STEELS A) S1-1200 AND B) S2-900.....	39
FIGURE 4.5-A) IMPACT ENERGY TRANSITION CURVE OF STEEL 1 AND B) FRACTURE APPEARANCE TRANSITION CURVE OF STEEL 1, C) IMPACT TRANSITION CURVE FOR STEEL 2, D) IMPACT TRANSITION CURVE OF STEEL 3.....	41
FIGURE 4.6- A), C), E) AND G) SE IMAGES OF COARSE TiN PARTICLES FOUND AT INITIATION SITES NEAR NOTCHES IN DIFFERENT HEAT TREATED SPECIMENS; B), D), F) AND H) HIGHER MAGNIFICATION IMAGE OF THE FIS OF A), C), E) AND G), RESPECTIVELY. ....	46
FIGURE 4.7-FRACTURE SURFACE OF S1-900, NO IDENTIFIABLE FEATURES CONSIDERED AS CRACK INITIATION SITES COULD BE OBSERVED .....	47
FIGURE 4.8-A CLEAVAGE FACET FOUND IN THE S3-1100 SPECIMEN, NO CLEAR CRACK INITIATING FEATURE WAS FOUND, WHICH SUGGESTS THAT THE CRACK MAY HAVE INITIATED FROM A GRAIN BOUNDARY CARBIDE.....	48
FIGURE 5.1-MNS AND Al <sub>2</sub> O <sub>3</sub> INCLUSIONS IN/ON A TiN PARTICLE WHICH INITIATED FINAL FAILURE OF S1-1200. A) FRACTURE SURFACE, IT CAN BE SEEN THAT A TiN PARTICLE IS ACTING AS THE FRACTURE INITIATION SITE BY TRACING THE “RIVER PATTERN”; B) A HIGHER MAGNIFICATION IMAGE OF THE TiN PARTICLE; C) EDS RESULT FOR POINT A IN IMAGE B), SHOWING THAT POINT A IS A MNS INCLUSION; D) EDS RESULT FOR POINT B IN GRAPH B), THE “BLACK CENTRE” OF THE TiN PARTICLE SHOWN TO BE A Al <sub>2</sub> O <sub>3</sub> INCLUSION. ....	57

*List of Figures*

FIGURE 5.2-A GRAIN-SIZED CRACK ARRESTED AT A GRAIN BOUNDARY BENEATH THE FRACTURE SURFACE OF S2-1100.....	58
--	----

# Chapter 1

## Introduction

Due to the ease of manufacture and low cost, structural steels are used in different environments with a wide range of working conditions. The two most important mechanical properties of these steels, strength and toughness, can be improved by a refinement in the grain size, whilst other strengthening mechanisms tend to reduce toughness. It is well known that due to the temperature sensitivity of their yield strength, metals with a body centred cubic (bcc) structure show a ductile-brittle transition behaviour that results in brittle fracture at low temperatures.

Alloying elements such as niobium, vanadium, and titanium are added to steels to improve strength and toughness by: pinning austenite grain boundaries during reheating (typically Ti(C,N) particles) to limit grain growth; controlling recrystallisation during hot deformation (typically Nb solute drag and Nb(C,N) particles); and forming a distribution of fine strengthening precipitates (typically VC particles)<sup>1</sup>. However, at the same time large ( $> 0.5 \mu\text{m}$ ) particles, that form during solidification, can cause crack initiation and propagation, for instance coarse TiN particles<sup>2,3</sup>.

It has been showed by many researchers<sup>2,4-7</sup> that coarse TiN particles, which can be defined as particles with a side length exceeding  $0.5 \mu\text{m}$ <sup>8</sup>, precipitate in the liquid steel and have a negative effect on the toughness in low alloy steels.

The main section of research presented in this thesis concentrates on three steels with different compositions, particularly Ti content. The aim of the work has been to identify how the coarse TiN particles and ferrite grain size affect the Charpy impact toughness of low carbon steels.

The effect of Ti in steel and the characterization of TiN particles are reviewed in Chapter 2, as well as the general effect of grain size on mechanical properties of steels, inclusion initiated fracture mechanisms, the reason that bcc materials show a ductile-brittle transition and equations to predict the ductile-brittle transition temperatures. The metallographic methods, heat treatment procedures and details of mechanical property tests carried out are included in Chapter 3.

The experimental results are presented in Chapter 4, including the microstructure characterization work, TiN particle quantification, comparison of predicted and experimental DBTT values and the fracture surfaces analysis by SEM. Further detailed fractographic analysis is presented in Chapter 5 identifying the cleavage initiation features, followed by a discussion on the effect of TiN particles, grain sizes and test temperature on the toughness behaviour.

The general conclusions that arise from this work are presented in Chapter 6 along with suggestions for further work.

# **Chapter 2**

## **Literature Review**

This section reviews the effect of titanium in steels, and the influence of microstructural features such as inclusions and grain size on the toughness of steels. The relevant literature on the effect of titanium in microalloyed low carbon steels has been investigated in section 2.1. In section 2.2, the effect of TiN particles on properties of steels is investigated. Section 2.3 reviews the effect of grain size on mechanical properties. Section 2.4 reviews the micromechanisms for cleavage fracture in steels contain disperse particles. Section 2.5 reviews the effect of microstructural features on fracture toughness and the mechanism of cleavage fracture related to coarse TiN particles.

### **2.1 Titanium in Steels**

The earliest use of titanium in iron or steel was for the purpose of removing oxygen from molten metal, that is, as a deoxidizer; deoxidation by titanium is as effective as aluminium deoxidation<sup>1</sup>. Besides, Ti in steels also have an effect on preventing susceptibility to strain-aging embrittlement as the same as Al<sup>1</sup>.

Titanium is a strong nitride and carbide forming element, and can form carbides and nitrides (sometimes also carbo-nitrides) usually with sodium chloride structure, which often have a high hardness and melting point<sup>9</sup>. If these nitrides and carbides in steels are fine (usually defined as smaller than < 0.5 μm), then they can improve hardness, abrasive wear resistance and fatigue strength of steels, besides, and the presence of such fine particles can also refine the grain size during high temperature processing by restricting the growth of austenite grains<sup>1</sup>.

Titanium can also form intermetallic compounds such as Ni<sub>3</sub>Ti and Ni<sub>2</sub>AlTi to strengthen steels (especially in the refractory and high-alloy steels such as maraging steels<sup>1</sup>).

Titanium can reduce the austenitic range in the Fe-Fe<sub>3</sub>C phase graph (Figure 2.1), both for the temperature and composition range, meaning that the addition of Ti can result in a contracted or even closed  $\gamma$ -phase field (also known as  $\gamma$ -loop <sup>10</sup>), shown in Figure 2.2, by compressing the temperature range that austenite can be present (lowering the HN line, at the same time lifting GS and PS line), and shifting the S point and E point in Figure 2.1 toward the upper-left corner. Besides, as mentioned above, titanium is a strong carbide forming element, which means with the presence of Ti, the diffusion activation energy of C in austenite is increased significantly, from these two points, the addition of Ti in steels can delay the incubation period for the pearlite transformation and shorten the incubation time for bainite compared with pearlite, so that bainite can be obtained by air cooling after austenization, as shown in Figure 2.3.

## 2.2 Titanium Nitride Particles

Nitrogen in solution can be an undesirable element in steel as it can cause quench aging and strain aging, which increases the strength and decreases the plasticity and toughness significantly. These disadvantages can be reduced by the addition of titanium (or aluminium), which can “fix” nitrogen in steel through the formation of TiN, which also prevents the occurrence of porosity caused by nitrogen <sup>1</sup>. Generally Ti is added to preferentially react with N to form TiN particles to give grain boundary pinning during high temperature processing.

### 2.2.1 TiN Particle Characteristics

Titanium nitride, which is known to be one of the most stable nitrides that form in steel, has a sodium chloride (fcc) structure with a lattice parameter of 0.423 nm and a cubic or rectangular-prism morphology <sup>11</sup>. Under an optical microscope, TiN has a golden colour for both etched and unetched samples. TiN often shows a so-called black-centre when it is combined with a Ti-oxide or alumina inclusion <sup>12</sup>, shown in Figure 2.4.

Since titanium is a very strong nitride former and TiN is formed before TiC during solidification, TiN tends to have a low solubility even at high temperatures <sup>9</sup>. It is reported that cubic or rectangular shaped precipitates exhibit higher efficiencies in pinning grain boundaries than other shaped precipitates <sup>13,14</sup> because the cubic particles usually exert a larger drag force on the boundary than spherical particles <sup>15</sup>. For these reasons, TiN particles may have the ability to pin grain boundaries and inhibit the growth of austenite grains during melting and solidification processes.

For TiN, there are two kinds of particles commonly seen in steels: fine particles are those which precipitate in the solid state and therefore have a fine size of 10-100 nm, these fine particles can pin austenite grain boundaries effectively; coarse particles are those that formed in liquid steel during the solidification process and have a size of 0.5-1  $\mu\text{m}$  or even larger, which prove not only ineffective in pinning grain boundaries but also can act as a cleavage origin in some steels <sup>2</sup>.

### 2.2.2 Solubility and Composition of TiN

#### a). Solubility product of TiN

The solubility product developed by Inoue and Dumitrescu <sup>16,17</sup> of TiN is:

$$\text{Log } ([\text{Ti}][\text{N}])_{\gamma} = 4.35 - 14890/T \quad \text{Eq.2.1}$$

where [Ti] and [N] are the Ti and N contents (wt%) dissolved in steel, T refers to temperature in K. From this equation, the solubility product of TiN in austenite ( $\gamma$  phase) under a certain temperature can be calculated. Besides, when using Eq.2.1 a premise can be made that all of the nitrogen dissolves in the austenite which implies that all of the titanium should also be dissolved in the austenite <sup>6</sup>. Under this premise, assuming the total Ti and N contents are given by  $\text{Ti}_{\text{tot}}$  and  $\text{N}_{\text{tot}}$ , then a critical temperature at which all of the titanium and nitrogen are dissolved in the steel (austenite) can be calculated as well.

Another equation given by Narita<sup>16</sup> is:

$$\text{Log } ([\text{Ti}][\text{N}]) = 5.9 - 16586/T \quad \text{Eq.2.2}$$

which indicates the stability of TiN particles formed in the liquid. It is obvious that Eq.2.1 and Eq.2.2 both have the same form but just slightly different numerical values, this could simply be due to the fact that these two equations are developed by different research groups, and certainly there were some difference between the compositions of steels they used.

This difference indicates that, different TiN particle stability could be given by using different experimental data as the presence of other alloy elements in steel. Therefore, the usage of thermodynamic software such as Thermal-Calc is necessary to provide the prediction of the stability of TiN particle for multi-component steels.

b). Influence of Ti/N ratio on the formation of TiN particles

TiN formation and the size and distribution of particles that form are also influenced by the Ti/N ratio. As mentioned above, only fine TiN particles can pin grain boundaries effectively and coarse particles can initiate cleavage fracture, thus, it is important to control the TiN particle size in steels, which can be done by controlling the Ti/N ratio.

It is reported by several researchers<sup>6,17,18</sup>, based on experimental work, that a Ti/N ratio of 1 (in at %) or 3.42 (in wt %) is beneficial in forming the desired finely dispersed TiN particles and the particle size will increase with a rise in Ti/N ratio.

In summary, both the TiN particle solubility temperature and Ti/N ratio have an influence on the formation of TiN, and particles formed in the liquid state are much larger and cannot be refined by fast cooling rates in the liquid steel<sup>8</sup>.

## 2.3 Effect of Grain Size on Mechanical Properties in Steels

The effect of ferrite grain size on strength is well established by the Hall-Petch relationship:

$$\sigma_y = \sigma_0 + k_y d^{-1/2} \quad \text{Eq.2.3}$$

where  $\sigma_y$  is yield strength,  $\sigma_0$  is lattice friction force which is supposed to be a constant for a certain material,  $k_y$  is a constant in connection with crystal structure, and depends on the steel,  $d$  refers to the average grain size <sup>19</sup>, then it can be seen obviously that the yield strength of material increases with the decreasing of average grain size.

The toughness of steels can be generally represented by the ductile-brittle transition temperature (DBTT)  $T_c$  and the impact energy  $\alpha_k$ , which is the energy absorbed during a impact test. A low  $T_c$  and a high  $\alpha_k$  often make a good toughness to steel. A relationship between  $T_c$  and grain size  $d$  indicated in the literature is:

$$T_c = T_0 - k_T d^{-1/2} \quad \text{Eq.2.4}$$

where  $T_0$  and  $k_T$  are constants for a certain material, so that the smaller the grain size  $d$ , the lower the  $T_c$ , which can be inferred as a higher toughness material <sup>20</sup>. Further discussion on the equations available in the literature to predict the DBTT are presented later.

## 2.4 Micromechanics for Cleavage Fracture

According to Griffith's cleavage fracture theory, cracks will become unstable only if the combination of stress level and crack size reaches the material fracture toughness <sup>21</sup>. Therefore, once a microcrack appears in the specimen (i.e. initial crack length is fixed), cleavage fracture will be only stress controlled, and if the tensile stress exceeds the critical value, the microcrack will propagate. After a grain or part of it reaches its plasticity limitation, a grain-sized crack will be

produced and may cause catastrophic cleavage fracture by propagating unstably depending on the conditions such as the temperature and the driving force.

After a grain-sized crack is produced, there are two different consequences for the crack. Firstly, in the ductile regime, the crack will be arrested at a grain boundary and its propagation stopped due to it being blunted under the deformation acting on it<sup>5</sup>, then separate cleavage facets surrounded by ductile fracture will appear on the fracture surface. However, the crack can also propagate across the grain boundary without being arrested or blunted in the brittle regime. In the brittle regime, cleavage fracture, which almost contains no plastic deformation of the material, will happen and the fracture surface will be totally brittle, the fracture initiation sites can be traced by following the “river pattern” of the fracture surface.

The reason that a grain-sized crack may develop in either the ductile regime or the brittle regime is the difference between the stresses that the crack may need to across a grain boundary, i.e. the strength of the matrix-matrix boundaries, which depending strongly on the interface energy. Due to the interface energy being a temperature-controlled factor, even for the same material with the same grain size, the fracture behaviour will be different depending on the temperature. At low temperature, due to the surface energy being very low, the strength of the matrix-matrix interface is poor, i.e. the critical fracture stress of the matrix is low, which can be easily reached to cause cleavage fracture to happen; but as the temperature increases, the surface energy will also significantly increase<sup>5,22</sup>, which leads to a good matrix-matrix strength, and results in a requirement of high loading to reach the critical fracture stress for cleavage fracture, if the stress is not high enough, the crack will be arrested and blunted at the grain boundary, so that ductile fracture will happen instead of brittle fracture.

## 2.5 Micro-crack initiated from TiN particles

The tessellated stresses, which arise from the difference between thermal-expansion coefficients of TiN particles ( $9.4 \times 10^{-6}$  mm/ $^{\circ}$ C) and the matrix ( $23.0 \times 10^{-6}$  mm/ $^{\circ}$ C for austenite and  $12.3 \times 10^{-6}$  mm/ $^{\circ}$ C for ferrite), will provide radial compressive stresses around TiN particles and circumferential tension stresses near the particle-matrix interface (shown in Figure 2.5 a)) as the TiN particles will shrink less than the matrix during cooling, and this tessellated loading can be sufficient intense to plastically deform the nearby matrix (suggesting that tessellated stresses at least have a magnitude of the yield strength)<sup>23</sup>, and are considered to be a key factor on crack nucleation from a TiN particle.

As shown in Figure 2.5 a), it can be seen that the matrix experiences radial compression and circumferential tension at the same time while the TiN particle only experiences a radial compression. Therefore, three main possible effects of tessellated stresses on TiN-initiated cleavage in steels<sup>23</sup> can be concluded as below:

First, the bond at the inclusion-matrix interface is enhanced by the compression in the matrix. Thus, the particle will not separate from the matrix easily due to a strengthened bond, and furthermore, this enhancement also allows cracks to transfer continuously and more efficiently between the particle and matrix.

Second, the crack propagation driving force is elevated. This is mainly because TiN particles often have different geometries (normally rectangular or triangle) and are distributed randomly in steels, for this reason the effect of tessellated stresses will be different according to the orientation of the particles, i.e. particles with a long side approximately perpendicular to the crack plane (or parallel to the loading direction) will experience a higher magnitude stress than those where the long side is

perpendicular to the loading direction, and moreover, this orientation of long side of the particle perpendicular to the crack plane will also provide the crack more opportunities to experience a tensile stress once it has nucleated in a TiN particle and will penetrate the matrix immediately due to the obvious circumferential tension along the long side of the particle-matrix interface.

Third, the radial compression imposes on the TiN particles a hydrostatic compression, which can lead to a higher magnitude of driving force when fracture occurs. For comparison, we can assume a circumstance where there is no hydrostatic compression in TiN, and the matrix strength is higher than particle strength. Under these circumstances, it is obvious that for the particles without hydrostatic compression, once the loading stress reaches the particle critical fracture strength, the particle will break and a microcrack will initiate from the broken TiN particle, but may be arrested at the particle-matrix interface or grain boundaries when propagating. However, for the particles with the radial compression around them, still considering particle strength < matrix strength, the particles will experience and be “protected” by this compression stress, which means, the crack cannot form easily in the TiN particle (nor propagate through the particle) when the loading stress is insufficient to neutralize the compression stress, therefore the required driving forces to break TiN particles are elevated and the toughness of the whole material is therefore improved slightly (fracture driving force is improved slightly). However, this increased stress to break the TiN particles may result in an undesirable consequence: once the loading stress is sufficient to break the TiN particle, which means the magnitude of this driving force is much higher, the microcrack formed by the broken TiN particle cannot be arrested at the particle-matrix interface or grain boundaries easily, therefore catastrophic crack propagation under this stress magnitude will be more likely to happen. This means that hydrostatic compression will make the failure of TiN particles more dangerous and critical during the fracture process.

According to previous research work <sup>4,8,24</sup>, it is believed that the pileup of dislocations formed in the matrix is one of the main factors to initiate microcracks around TiN particles (shown in Figure 2.5 b)), due to the lattice microstructure (NaCl-type), which related to the dislocation slip systems and ductility of TiN particles, is different from the matrix, therefore the dislocations formed in matrix cannot transfer easily into the particles, then the dislocations will produce microcracks around the particle-matrix interface. The other factor that affects the initiation of microcracks is the stress concentration caused by TiN particles due to its rectangular shape.

## 2.6 Critical processes in TiN particle initiated cleavage fracture

According to previous research work <sup>5,8,23-25</sup>, a model for TiN initiated cleavage fracture can be established. There are three critical steps involved in a TiN particle initiated cleavage fracture process: first, microcrack nucleation at a TiN particle; then the microcrack penetrates the matrix across the particle-matrix interface and grows into a grain-sized crack; thirdly, the grain-sized crack continues to propagate across the grain boundaries and becomes unstable, resulting in catastrophic cleavage fracture.

Whether the fracture is crack nucleation dominated or propagation dominated is significant, if the fracture is nucleation dominated, it is almost impossible to prevent the crack propagation once it formed, then catastrophic cleavage fracture will happen; on the other hand, if the fracture is propagation dominated, then it will be easier to prevent the crack from growing too large and improve the material's toughness.

According to the fracture stress analysis theory <sup>23-25</sup>, whether the fracture is nucleation or propagation dominated can be known by analyzing the stress states of the material. Figure 2.6 shows the general trend of the variation of fracture strengths (ferrite grain strength, particle strength, yield strength and peak stress in the plastic zone around the crack tip) at different temperatures, and

the regions of nucleation control and propagation control can also be identified in the graph by comparing the strength values at a fixed temperature.

As shown in the Figure 2.6, at the lower temperatures, particle cleavage strength and ferrite grain strength are both lower than the yield stress and peak stress in the plastic zone, therefore, once the stress exceeds the particle cleavage strength, the crack will appear in the broken particle and start to propagate, then resulting in the final failure of material; when the temperature is higher, the particle strength exceeds both the yield strength and ferrite grain strength but is still lower than the peak stress in the plastic zone, therefore the crack will still form in broken particles, but whether it will propagate into the matrix or not depends on the criterion for propagation across the particle-matrix interface; as the temperature increases, the ferrite grain strength will exceed both the particle cleavage strength and yield strength but be lower than the peak stress in the plastic zone, then the crack initiated from particles will not be able to cross the first grain boundary unless the criterion for propagation across the matrix-matrix boundary is fulfilled; at the highest temperatures, as both ferrite grain strength and particle cleavage strength exceed the peak stress in the plastic zone, cracks cannot form in either the particles or matrix, and the failure of the material will be ductile fracture.

## 2.7 Ductile-brittle transition temperature (DBTT)

Body-centred cubic (bcc) metals show an obvious ductile to brittle transition as the temperature decreases while face-centred cubic (fcc) metals tend to maintain good ductility at all temperatures. The reason behind the transition shown by bcc metals is based on the increase in yield strength and significant decrease in ductility at low temperature compared to fcc metals, therefore the critical resolved shear stress ( $\tau_s$ ) or yield strength ( $\sigma_y$ ) of the material increases significantly and can exceed the critical cleavage stress ( $\sigma_f$ ) or ultimate tensile stress ( $\sigma_{UTS}$ ) easily as the temperature

decreases (shown in Figure 2.7), and the energy absorbed by the material is limited and cleavage fracture happens.

The ductile-brittle transition is affected by several factors: a) low temperatures, which cause the increase in yield strength, b) high strain rates, which also increase yield stress, c) notches (or fatigue cracks), which cause local stress concentration and a triaxial stress state around the notch and d) particular crystal structures and microstructure.

To determine the transition behaviour, a series of impact tests such as Izod and Charpy tests is often used for material evaluation and quality control. In both cases a notched specimen is struck by a swinging pendulum released from a fixed height, with the absorbed energy being used to produce the toughness curve (shown in Figure 2.8).

Figure 2.8 shows typical impact test curves (absorbed impact energy versus test temperature) for different materials. It can be seen that fcc metals show a high absorbed energy across the temperature range while high strength alloys and ceramics maintain low toughness at all temperatures, and the absorbed energy of bcc metals decreases as the test temperature decreases. For the bcc transition curve, the temperature where the absorbed energy reaches a level equal to the average of the upper and lower shelf values is commonly defined as the ductile-brittle transition temperature (DBTT).

## 2.8 Predictions of DBTT

The Gladman-Pickering equation <sup>26</sup> (presented as Eq.2.5) can be used to make predictions of the DBTT of ferrite steels:

$$\text{DBTT} = -19 + 44 \text{ pct Si} + 700N_f^{0.5} + 2.2 \text{ pct pearlite} - 11.5d^{-0.5} \quad \text{Eq.2.5}$$

where pct Si is the weight percentage of silicon in steel,  $N_f$  is free-nitrogen content (in wt pct), pct pearlite is pearlite area percentage in steel and  $d$  is ferrite grain size (in  $\mu\text{m}$ ).

However, it has been found that this equation does not predict accurately when there are other alloy elements in steels and grain boundary carbides precipitate<sup>26</sup>. Therefore, Mintz<sup>27,28</sup> developed another equation, which makes predictions of DBTT values successfully for ferrite-pearlite steels:

$$DBTT = 112t^{0.5} - 13.7d^{-0.5} + 15 \text{ pct pearlite}^{0.33} + 0.43\Delta Y + 20 \quad \text{Eq.2.6}$$

where t is the grain boundary carbide thickness (in  $\mu\text{m}$ ), d is the average grain size of ferrite, pct pearlite is the amount of pearlite (area %) in the steel,  $\Delta Y$  is the precipitation-hardening component (Eq.2.7), which is calculated from the differences between the measured yield strength at room temperature ( $\sigma_{YS}$ ) and the non-precipitation-hardened yield strength ( $\sigma_{np-YS}$ , according to Eq.2.8):

$$\Delta Y = \sigma_{YS} - \sigma_{np-YS} \quad \text{Eq.2.7}$$

and  $\sigma_{np-YS}$  can be determined from the following relationship:

$$\sigma_{np-YS} = 43.1 \text{ pct Mn} + 83 \text{ pct Si} + 15.4d^{-0.5} + 1540 \text{ pct N}_f + 105 \quad \text{Eq.2.8}$$

where  $N_f$  is the free-nitrogen content (in wt pct) which was taken as zero due to the high microalloy content in these steels in this work, according to previous research<sup>8</sup>.

However, it should be noted that the Mintz equation (Eq.2.6) has limitations in validity based on the composition of materials it was developed for, previous research work<sup>28</sup> suggested that this equation is best applied on steels containing (all in wt %): 0.11-0.20 C, 0.63-1.56 Mn, 0.02-0.49 Si, 0.003-0.021 N, Nb up to 0.071, Ti up to 0.16, V up to 0.20 and Al up to 0.12.

## 2.8 Overall summary of steel toughness affected by coarse TiN particles

There is a lot of evidence showing that coarse TiN inclusions can act as fracture initiation sites in steels; Table 2.1 shows details where coarse TiN particles have been suggested to affect toughness, including the size of the TiN particle observed to act as the cleavage initiation site and the average grain size (in some cases prior austenite, PA, size) of the material.

Even though TiN particles have been observed to act as cleavage crack initiators, the toughness variation has not been linked with both grain size and particle size (or particle number density)<sup>7,8</sup>.

Therefore, the relationship between TiN particle size distribution and grain size is not clear and there is still no comprehensive study in this area reported.

Table 2.1. Literature data on the role of TiN on fracture in steels

Main composition	Microstructure	Grain size/ $\mu\text{m}$	Cleavage initiating TiN particle size/ $\mu\text{m}$	TiN acts as initiation site or not	Test method	DBTT/ $^{\circ}\text{C}$
0.37%C, 0.0162%N, 0.015%Ti <sup>2</sup>	ferrite + pearlite	5.5 (ferrite)	3.3	Yes	CVN Impact test	65
0.23%C, 0.0075%N, 0.044%Ti <sup>3</sup>	ferrite + pearlite	19.8 (ferrite)	3.2	Yes	4PB test	N/A
0.052%C, 0.0062%N, 0.026%Ti <sup>6,24</sup>	ferrite + bainite	50 (PA*)	5	Yes	CVN Impact test	>15
0.093%C, 0.0045%N, 0.045%Ti <sup>7</sup>	upper bainite	100 (PA*)	4	Yes	CTOD	>RT
0.089%C, 0.0048%N, 0.1%Ti <sup>8</sup>	ferrite + bainite	110 (PA*) 32 (PA*)	6.5 5.5	Yes Yes	CTOD	20 -50

\*PA: Prior Austenite grain

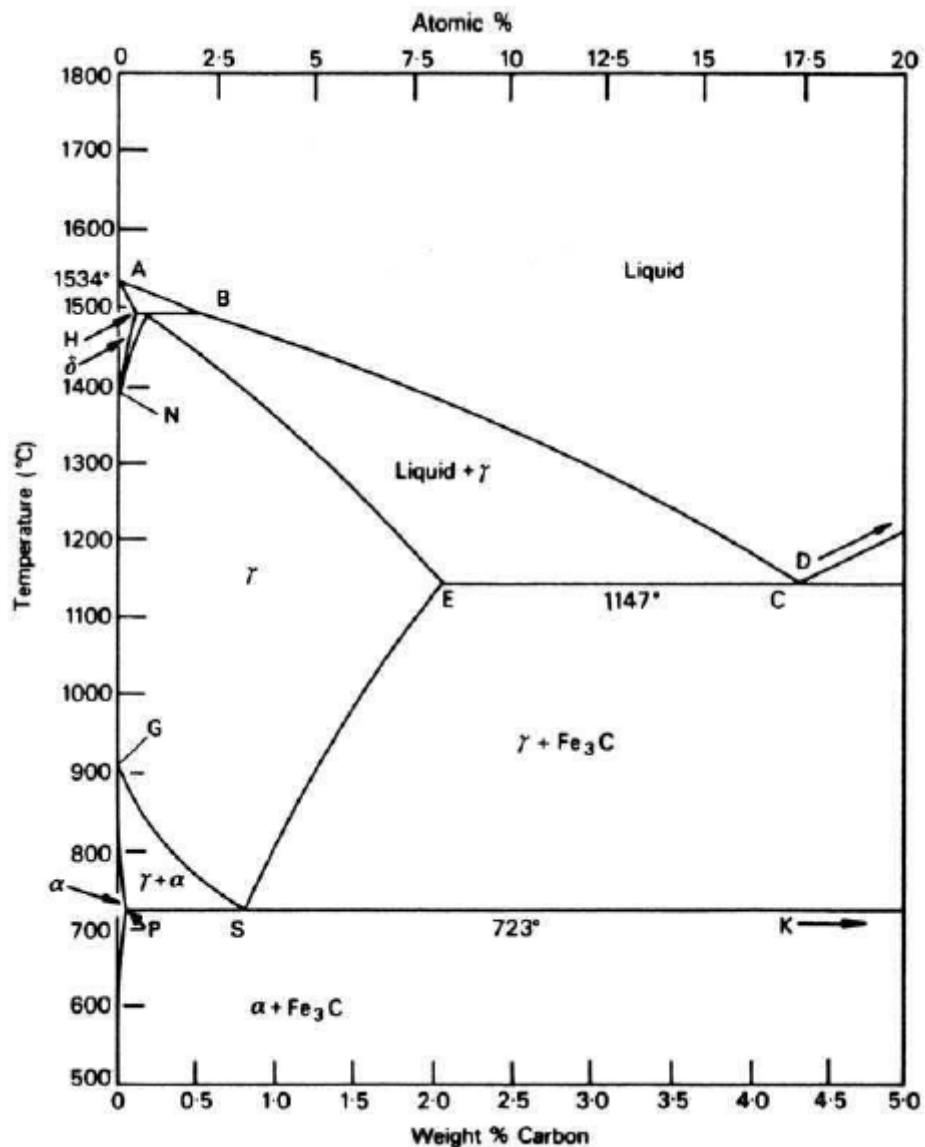


Figure 2.1-Fe-Fe<sub>3</sub>C phase diagram<sup>10</sup>.

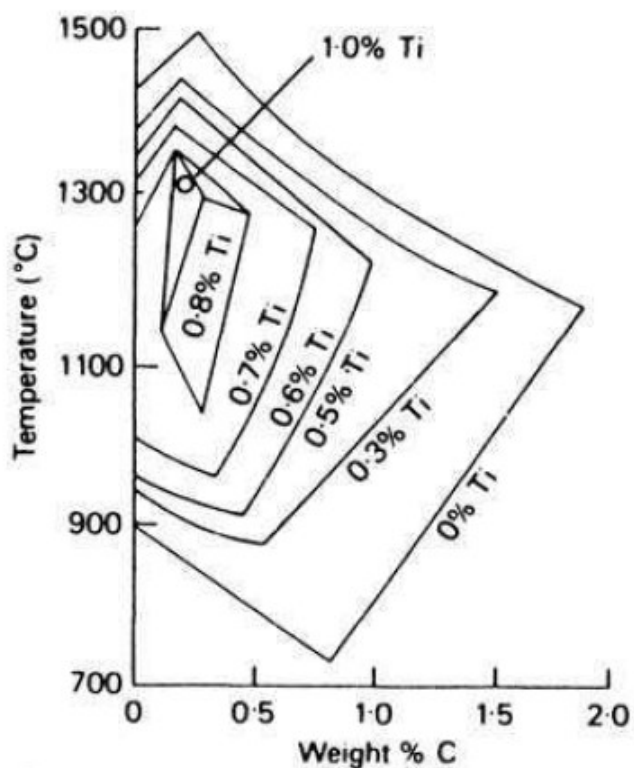


Figure 2.2-Effect of titanium on the  $\gamma$ -phase field<sup>10</sup>

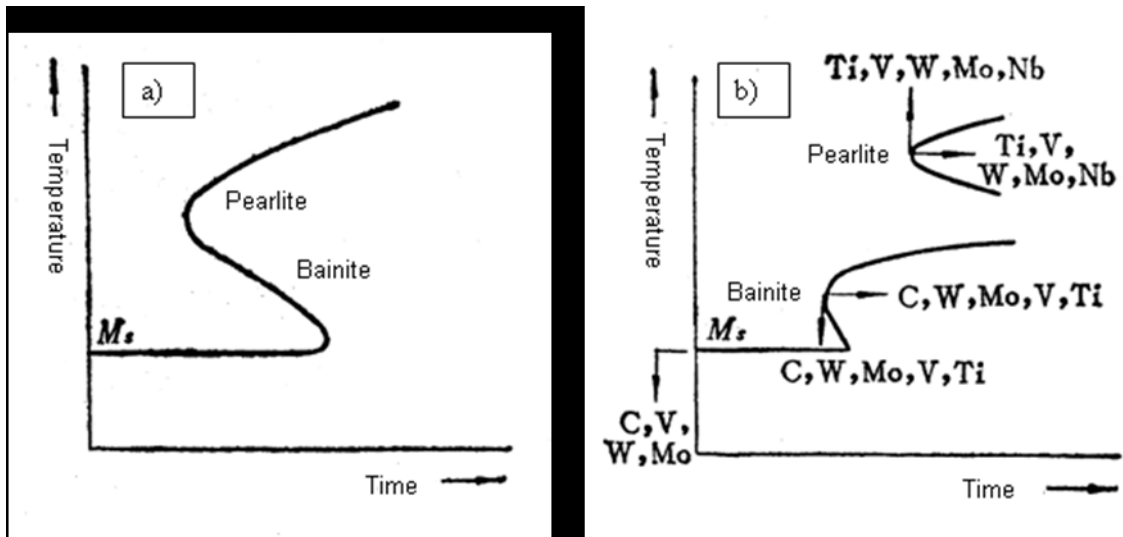


Figure 2.3-Effect of alloy elements on TTT curve of steel: a) Original TTT graph and b) effect of different alloy elements <sup>19</sup>.

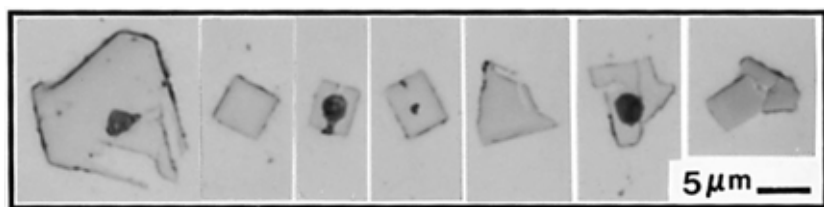


Figure 2.4-Shape of large TiN inclusions under an optical microscope, note that  $Al_2O_3$  particles (dark) can be observed in some TiN inclusions <sup>4</sup>.

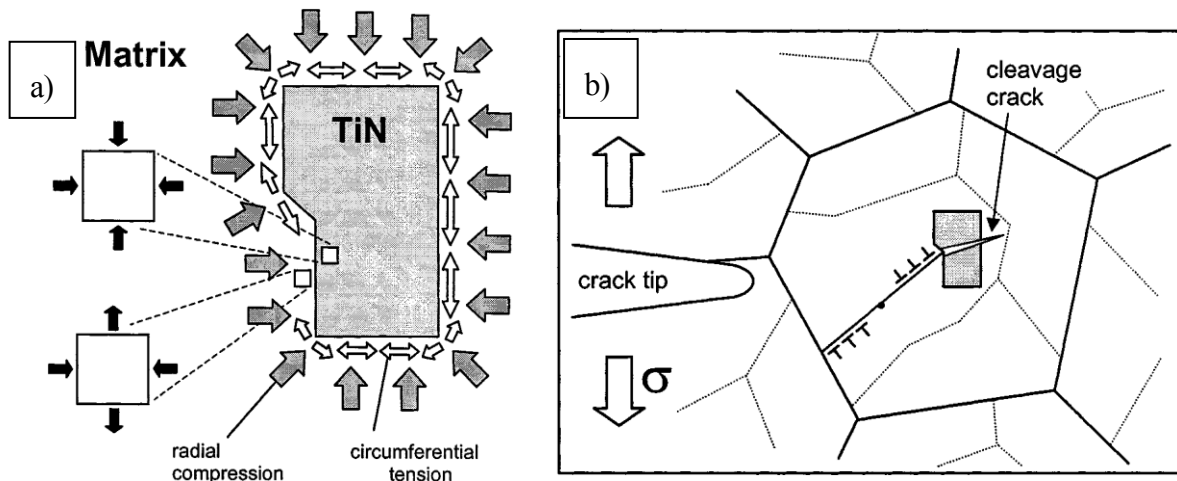


Figure 2.5-a) Tessellated stress distributions around a TiN particle and b) dislocation pile-up around a TiN particle to initiate microcrack<sup>23</sup>.

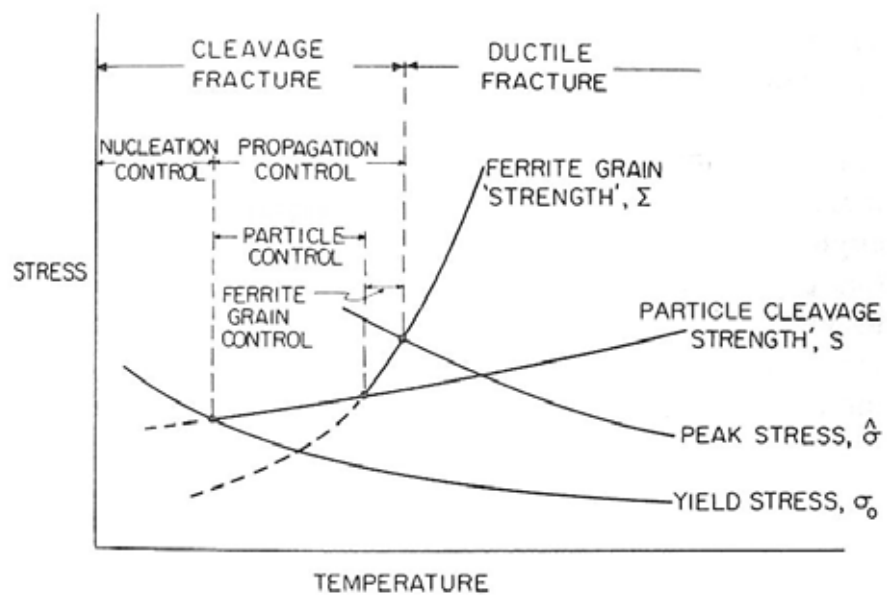


Figure 2.6-Variation of cleavage fracture strengths at different temperatures<sup>23</sup>.

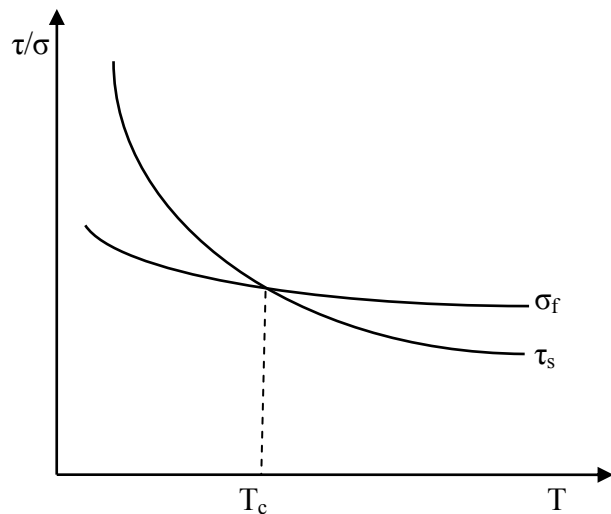


Figure 2.7-The effect of temperature on the critical cleavage fracture stress and critical resolved

shear stress of single crystal pure iron<sup>21</sup>.

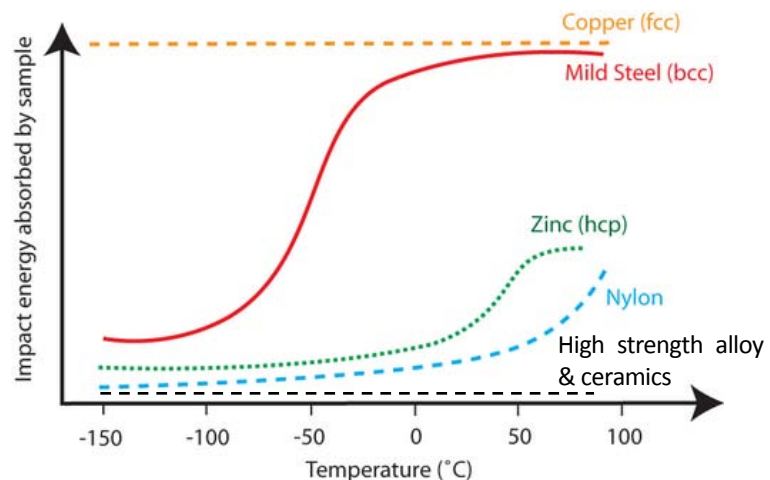


Figure 2.8-Impact transition curves for different materials<sup>21</sup>.

# Chapter 3

## Experimental Methods

### 3.1 Materials

Three steels were provided by Tata Steel plc, with compositions listed (supplied by the provider) in Table 3.1. Steel 1 is a TMCR (Thermo-Mechanically Control Rolled) high strength low alloy steel (30 mm thick) with a carbon content of 0.093 wt % and highest Ti content of the three steels examined; Steel 2, a thin plate (15 mm thick), was provided in the quenched then tempered condition after rolling and has a higher carbon content of 0.135 wt %, and contains higher levels of Al and V but with reduced Ti and Nb compared to Steel 1; Steel 3 is a TMCR steel (30 mm thick) and has the lowest Ti content but otherwise a similar composition and processing conditions to Steel 1 except for increased Ni. Both original heat treatments of Steel 1 and 3 are unknown.

Table 3.1 Compositions of steels investigated (wt %)

	C	Si	Mn	P	S	Ni	Mo	Cr
Steel 1	0.093	0.01	1.5	0.01	0.002	<0.02	<0.005	<0.02
	Cu	Al	Nb	V	Ti	N	B	-
	<0.02	0.026	0.05	<0.005	0.045	0.0045	-	-
	C	Si	Mn	P	S	Ni	Mo	Cr
Steel 2	0.135	0.35	1.33	0.012	0.001	0.02	<0.005	0.03
	Cu	Al	Nb	V	Ti	N	B	-
	0.01	0.037	0.027	0.054	0.027	0.0046	0.002	-
	C	Si	Mn	P	S	Ni	Mo	Cr
Steel 3	0.087	0.36	1.44	0.01	0.003	0.50	<0.004	0.011
	Cu	Al	Nb	V	Ti	N	B	-
	0.004	0.041	0.023	0.004	0.006	0.0061	-	-

### **3.2 Heat Treatment Methods**

The steels were heat treated to obtain ferrite-pearlite structures, with different ferrite grain sizes, to provide the same matrix microstructure so that the influence of TiN particles and ferrite grain size on toughness could be assessed.

The heat treatment processes are shown in Figure 3.1. The samples were placed in the centre of a hot furnace, and surface temperatures of samples were measured by a thermocouple equipped with a digital reader during heat treatment processes (including cooling processes).

For Steel 1, samples were heat-treated at 900 °C, 1100 °C and 1200 °C (defined as S1-900, S1-1100 and S1-1200), and then furnace cooled to room temperature. A similar procedure was used for Steel 3, heat treating to 1100 °C and 1200 °C (S3-1100 and S3-1200). A varied heat treatment method was used for Steel 2, due to the different as-received condition (thin plate), which was to spherodise at 680~690 °C for 12 hours to avoid banded structure after austenising, then austenitised at 900 °C or 1100 °C for 30 minutes followed by furnace cooling till around 500 °C then air cooled (S2-900 and S2-1100). During each heat treatment process, small samples ( $10 \times 10 \times 10 \text{ mm}^3$ ) of the three steels were used to determine the correct heat treatment temperatures and investigate the microstructures, and then larger blocks were heat treated for subsequent Charpy sample machining.

### **3.2 Metallography and image analysis**

After the heat treatments, characterization of the ferrite grain size, TiN particle size and distribution, and pearlite amount quantifications, were done on a Carl Zeiss optical microscope using ground, polished and etched (using 2% nital) samples; the grain size was measured by a mean linear intercept method from a total of 2000 grains for each sample and TiN particle size was measured as the maximum side length<sup>8</sup>.

In addition, Thermo-Calc software was used to predict the liquid temperatures and the precipitation temperatures of TiN particle in three steels, for analysing whether coarse TiN particles would present or not.

### **3.3 Scanning electron microscopy**

A Philips XL-30 scanning electron microscope equipped with Oxford INCA energy dispersive X-ray spectroscopy (EDS) was used to investigate the grain boundary carbide thickness and broken Charpy sample fracture surfaces.

Grain boundary carbide thickness,  $t$ , which was used to make the prediction of DBTT values in Eq.2.6, was measured using Mintz's method <sup>10,27</sup>, i.e. to measure the largest through thickness values of each carbide then calculate an average value, and the average values of around 80-100 carbides were taken as the  $t$  values for each sample, according to the method used in previous research work <sup>27,28</sup>.

Fracture surfaces and samples sectioned through the fracture surface were also analyzed; the broken specimens were coated with a thin nickel layer, using a nickel plate in Watt Bath liquid for around 20 min at 46 to 70 °C, and then sectioned, mounted, polished and etched. The cleavage initiation sites were investigated by tracing the river patterns on the cleavage facets. For the samples with fracture surfaces that were 100% brittle, the overall cleavage fracture initiation sites (FISs), which can be defined to be initiation sites that cause final failure of the sample <sup>8</sup>, and the local cleavage initiation sites (CISs), which can be defined to be initiation sites that cause local cleavage fracture within a small area without initiating final fracture <sup>8</sup>, were examined in the SEM. After the investigation of FIS and CIS, it was found that there were typically several FISs close to the notch and many more CISs compared to FISs throughout the fracture area.

### 3.4 Hardness tests and yield strength values

Vicker's macrohardness tests were performed with a load of 20 kg on the heat treated samples at room temperature on polished samples. Due to the limited amount of material available, the yield strength of each steel,  $\sigma_{ys}$ , which is required for predicting the DBTT values, was calculated according to the following relationship<sup>8,29,30</sup>:

$$\sigma_{ys} = k \times H_v \quad \text{Eq.3.1}$$

where  $k$  is a constant between 2.9 to 3.5, and in this work,  $k = 3$  has been used, which is the value determined experimentally in previous research on Steel 1 and 3<sup>8</sup>.

### 3.6 Charpy impact tests

To establish the relationship between grain size, TiN particle distribution and impact transition temperature, standard Charpy V-notch (CVN) test bars (as shown in Figure 3.2) were machined and the Charpy impact tests performed at different temperatures with the data used to plot impact energy transition curves according to the ASTM standard<sup>31</sup>.

Experimental temperatures were from -115 °C to 90 °C, obtained using a controlled mix of ethanol and liquid nitrogen, and with the temperatures measured by a thermocouple and electronic thermometer.

For bcc materials, the fracture mode changes from ductile to brittle when the test temperature decreases. The transition temperature can be defined as a ductile-brittle transition temperature (DBTT), which can be obtained according to the change in absorbed energy with the change of temperature. For impact tests, the DBTT value can be given as the temperature of the midpoint value between the upper shelf and lower shelf energies. Besides, the 50% FATT (Fracture Appearance Transition Temperature), which is defined as the temperature that 50% brittle fracture appears, can also be used to present the DBTT value<sup>21</sup>.

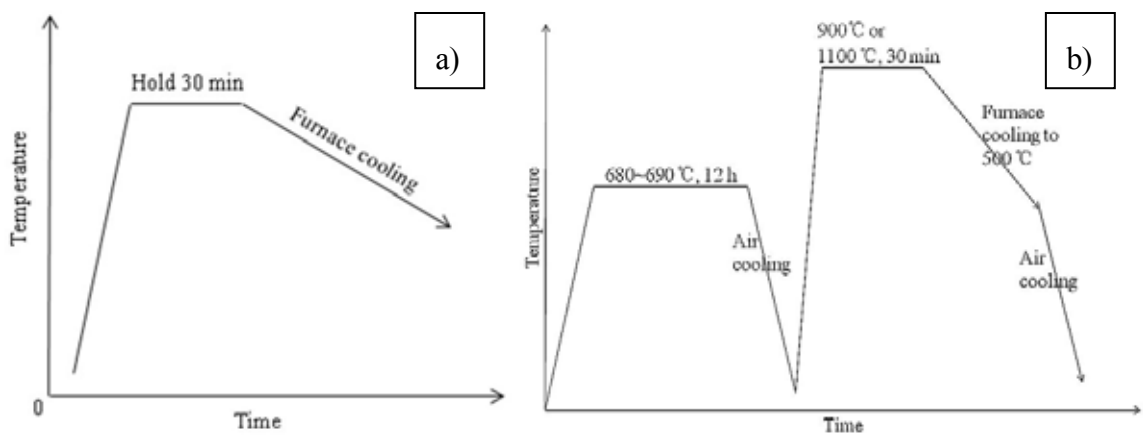


Figure 3.1-Heat treatment methods a) for Steel 1 and 3, b) for Steel 2

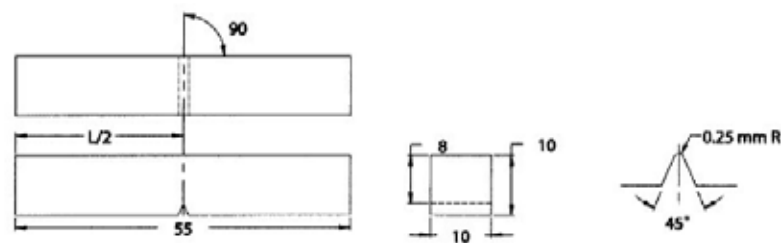


Figure 3.2-Standard Charpy V-Notch Specimens

# Chapter 4

## Results

### 4.1 Optical microstructure

Figure 4.1 shows the ferrite-pearlite microstructure of the three steels after heat treatments, it is obviously that the grain size increases with the increase of heat treatment temperature, shown in Figure 4.1.

The average ferrite grain size and pearlite content after heat treatment of the three steels are given in Table 4.1. It can be seen that the increasing heat treatment temperature results in a larger ferrite grain size as expected. The grain size distributions were unimodal for all heat treatment temperatures (shown in Figure 4.2).

Table 4.1. Grain size and pearlite amount for the different samples.

Material	Characterizations	Heat Treated Temperature / °C		
		900	1100	1200
Steel 1	Average Grain Size / $\mu\text{m}$	$5.0 \pm 2.4$	$13.2 \pm 1.9$	$27.3 \pm 3.1$
	Pearlite amount / area %	3.2	5.4	6.8
Steel 2	Average Grain Size / $\mu\text{m}$	$9.5 \pm 1.5$	$25.4 \pm 2.2$	--
	Pearlite amount / area %	6.8	10.2	--
Steel 3	Average Grain Size / $\mu\text{m}$	--	$16.2 \pm 2.7$	$28.4 \pm 3.4$
	Pearlite amount / area %	--	2.2	3.0

## 4.2 TiN particle investigation

For the steels investigated, according to Thermo-Calc, Steel 1, 2 and 3 have a TiN formation temperature of 1507 °C, 1484 °C and 1430 °C respectively, which, for both of Steel 1 and 2 is about 20 °C higher than the final solidification temperature and for Steel 3 it is 50 °C lower than the solidification temperature. In addition, Steel 1 and Steel 2 have a Ti/N ratio of 10 and 5.87 respectively, while Steel 3 has a much lower Ti/N ratio of 1, all of which indicate that coarse TiN particles should only appear in Steel 1 and 2, which matches with the result from the TiN particle characterization work.

TiN inclusions typically have a cubic or rectangular-prism morphology <sup>11</sup> and show a golden colour in an optical microscope; they are often found with a black-centre, which is considered to be a Ti-oxide or Al-oxide inclusion <sup>12</sup>. Figure 4.3 shows a typical TiN particle, which has formed on an Al<sub>2</sub>O<sub>3</sub> particle, along with the EDS compositions, in the steels investigated in this work. It can be seen that the particle contains Nb as well, this is expected to be primarily from Nb(C,N) precipitating on the TiN particle during cooling. Both Steel 1 and 2 were observed to contain coarse TiN particles, and around 30% of these TiN particles were observed to have aluminium oxide cores, also, around 80% of EDX traced TiN particles showed the presence of Nb.

For each of Steel 1 and Steel 2, around 120 coarse TiN particles were examined using an optical microscope; the average size and number density are displayed in Table 4.2, no coarse TiN particles were found in Steel 3. According to previous work <sup>8</sup>, there is no significant change in the coarse TiN particles when the steel is heat treated under 1350 °C, therefore the data from the as-received plate was used when analyzing the heat treated samples.

Table 4.2. Coarse TiN particle size and number density in the investigated steels

Materials	Ti/N ratio	Average size/ $\mu\text{m}$	Largest particle size/ $\mu\text{m}$	Number density/ $\text{mm}^{-2}$
Steel 1	10.00	$1.6 \pm 0.9$	4.2	88
Steel 2	5.87	$3.5 \pm 1.1$	6.5	14

It can be seen from Table 4.2, Steel 1 has a much higher number density of TiN inclusions than Steel 2 due to its higher Ti/N ratio and high Ti content, and this will result in a high frequency of occurrence of coarse particles around the Charpy notch, in the region of high stress concentration and hence may contribute to the final failure of the material by acting as fracture initiation sites. However, as the TiN particles in Steel 1 are smaller in average size, and have a smaller maximum size, the stress required to initiate cleavage from a particle will be higher, which would reduce their effectiveness.

### 4.3 Hardness and Strength

At least 5 macro-hardness values were used to determine the average  $H_V$  of each sample, and the yield strength of each heat treated sample was calculated using Eq.3.1. Results from hardness testing and the calculated yield strength are shown in Table 4.3 (with standard deviation).

Table 4.3. Macro-hardness ( $H_V$ ) Values and predicted yield strength of the Heat Treated Samples

Materials	Heat treated temperature/ $^{\circ}\text{C}$	Hardness ( $H_V$ )	Yield Strength ( $\sigma_{ys}$ )/MPa
Steel 1	900	$143.3 \pm 0.7$	$424 \pm 2.1$
	1100	$130.5 \pm 0.7$	$392 \pm 2.1$
	1200	$155.6 \pm 1.0$	$467 \pm 3.0$
Steel 2	900	$158.9 \pm 3.0$	$477 \pm 9.0$
	1100	$163.3 \pm 2.7$	$490 \pm 8.1$
Steel 3	1100	$146.8 \pm 2.6$	$440 \pm 7.8$
	1200	$154.9 \pm 1.4$	$465 \pm 4.2$

#### 4.4 Grain Boundary Carbide Thickness

Figure 4.4 shows the typical grain boundary carbides found in this work. The average size of between 80 and 100 carbides was calculated from SEM measurements for each steel (shown in Table 4.4); these were used as the  $t$  values in Eq.2.6 to make predictions of the ductile-brittle transition temperatures.

Table 4.4. Grain boundary carbide thickness ( $t$ ) of the steels investigated ( $\mu\text{m}$ )

	Steel 1			Steel 2		Steel 3	
Heat treatment temperature/ $^{\circ}\text{C}$	900	1100	1200	900	1100	1100	1200
Grain boundary carbide thickness ( $t$ )/ $\mu\text{m}$	0.07	0.11	0.18	0.07	0.08	0.09	0.12

## 4.5 DBTT Values

The Charpy impact data, as fracture energy and fracture appearance transition curves, are shown in Figure 4.5. Unfortunately, due to a limited number of samples from Steel 1 being available, the transition curve for S1-1200 specimens was incomplete; the Fracture Appearance Transition Temperature (FATT) curve has been extrapolated to obtain the 50% FATT. As the 50% FATT is very close to the DBTT in the same material<sup>21</sup>, this value was also used as the DBTT value in the subsequent analysis. For Steel 2 and 3, DBTT values are acquired from the energy transition curves, in these cases it was found that the DBTT and the FATT were in close agreement (FATT is around 5-10 °C higher than the DBTT<sup>21</sup>).

As can be seen from the transition curves, the ductile-brittle transition temperature of each sample increases with the increase of heat treatment temperature, related strongly with the increase in ferrite grain size.

The difference between the experimental and predicted DBTT values was calculated and presented as  $\Delta$ DBTT, which, as the Mintz equation doesn't take the effect of TiN into consideration, has been used to investigate whether the presence of coarse TiN particles has affected the DBTT. The experimental and predicted results are displayed in Table 4.5 (there would be a 10°C difference between predicted and experimental values due to the error of measurement).

Table 4.5. Comparison of Experimental and Predicted DBTT Values

	Steel 1			Steel 2		Steel 3	
HT Temperature/°C	900	1100	1200	900	1100	1100	1200
Experimental DBTT/°C	-105	-20	105	8	85	-15	40
Predicted DBTT by Eq 2/°C	-107	-35	100	-8	84	18	75
$\Delta$ DBTT/°C	+2	+15	+5	+16	+1	-33	-35

It can be seen that the DBTT for S1-900, S1-1200 and S2-1100 are well predicted, but for the S1-1100, S2-900 samples and all the samples of Steel 3, there are some difference between the experimental values and predicted values. As mentioned before, Eq.2.6 is only valid within a certain range of compositions, in the present work, only Steel 2 has a composition in this range, with Steel 1 having a slightly lower C and Si content and Steel 3 having a lower C content. The differences are relatively small, however, this may lead to inaccurate predictions for Steel 1 and 3. However, the  $\Delta$ DBTT values could also reflect inaccuracies in the measured values (due to the limited number of test specimens) or that TiN particles are having an influence on the toughness, which is discussed later.

A consistent disagreement between the predicted and experimental DBTT values arose when using the equation for Steel 3. It can be seen from Table 4.5 that the predicted values are higher than the experimental ones. It is proposed that this difference is due to Steel 3 containing a higher nickel content (0.50 wt %) than the other two steels (both up to 0.02 wt %). Nickel, which is an austenite stabilizer, is a solid-solution strengthener, and often promotes high toughness of steels<sup>32</sup> and is not accounted for by the Mintz equation, as this was derived for steels that did not contain Ni. It should be noted that Steel 3 does not contain any coarse TiN particles and was used in this investigation to determine if the Mintz equation accounts for the DBTT shift due to grain size changes, which it clearly does.

In order to investigate this behaviour the fracture surfaces were analysed.

## **4.6 Fracture Surface Analysis**

The brittle fracture area is composed of fracture facets and there are often identifiable fracture initiation sites (FIS) that cause final failure of the specimen, as well as local cleavage initiation sites (CIS) that cause local cleavage facets. FIS and CIS are located by tracing the path of river lines on

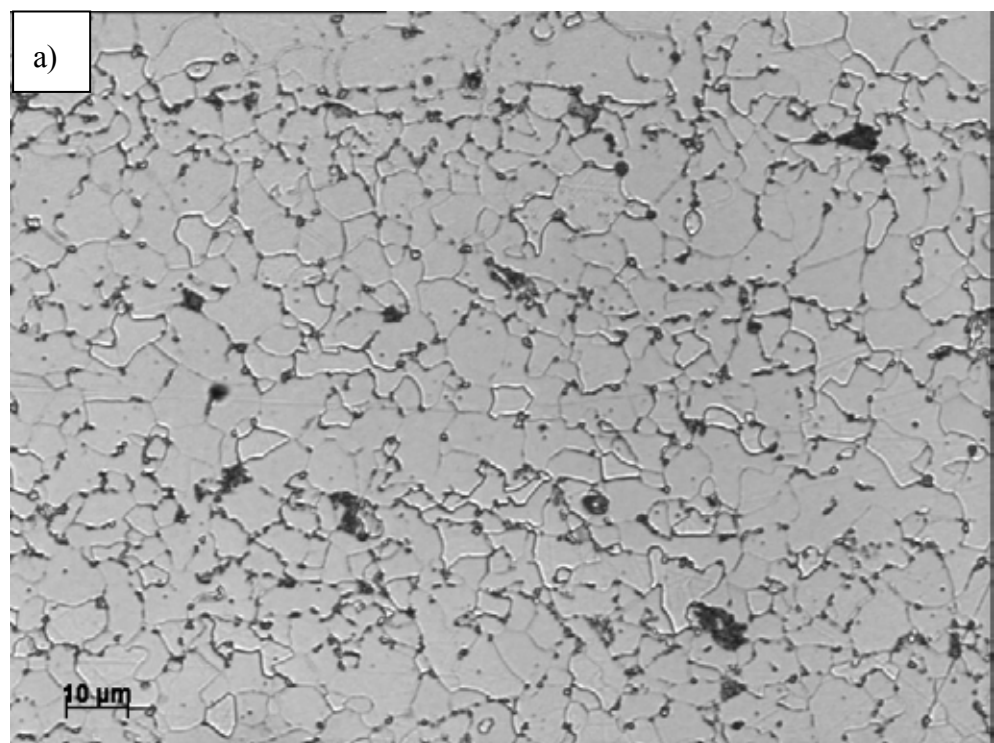
the fracture surface. No TiN fracture initiation sites were observed in Steel 3 samples, as no coarse TiN particles form in this steel. For Steels 1 and 2 it was only for S1-900 that there were no clearly identifiable CIS or FIS initiated by TiN particles found, while in all the other samples CIS and FIS associated with TiN were observed.

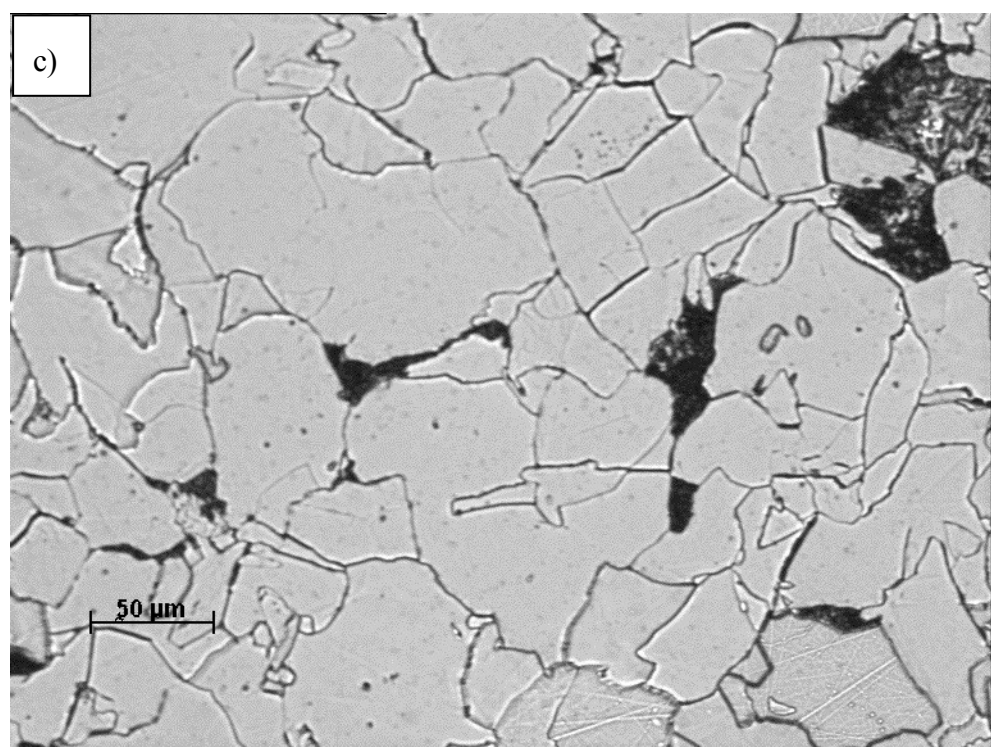
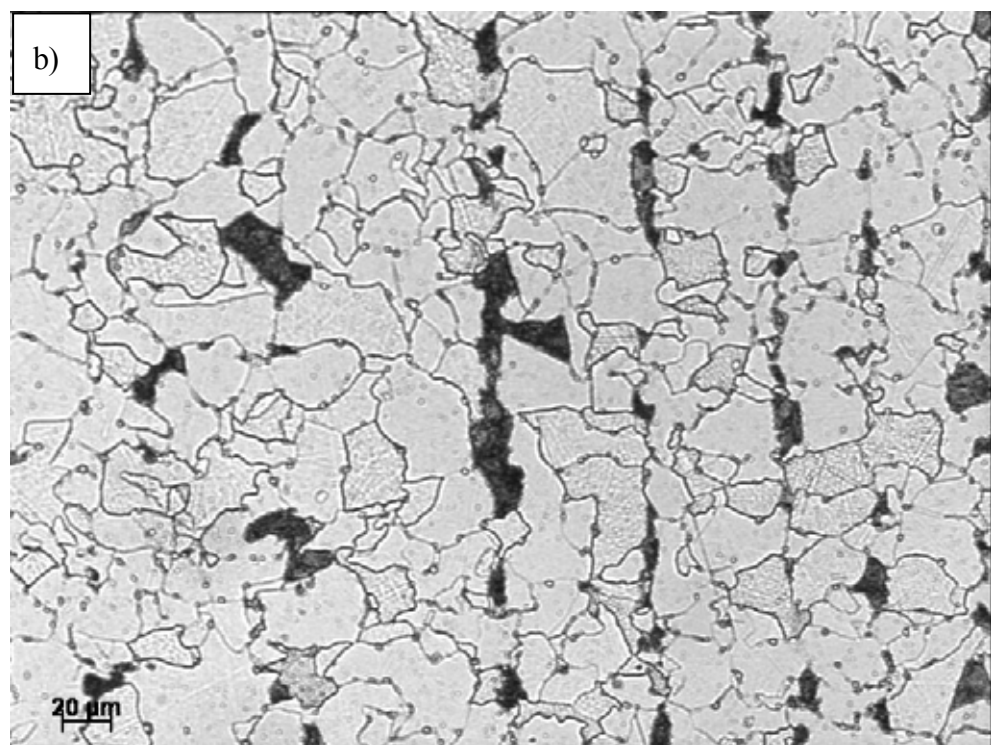
SEM photographs of FIS initiated from coarse TiN particles (chemical composition of the particle was determined by EDS) are shown in Figure 4.6. By following the “river patterns”, coarse TiN particles, which were located very close to the Charpy notches (30-400 $\mu\text{m}$ ), were determined to cause the final failure of the whole specimen. However, there were around 4 FIS in each low temperature broken specimen of Steel 1 but only around 2 for Steel 2, which is considered mainly due to the large number density of coarse TiN particles in Steel 1.

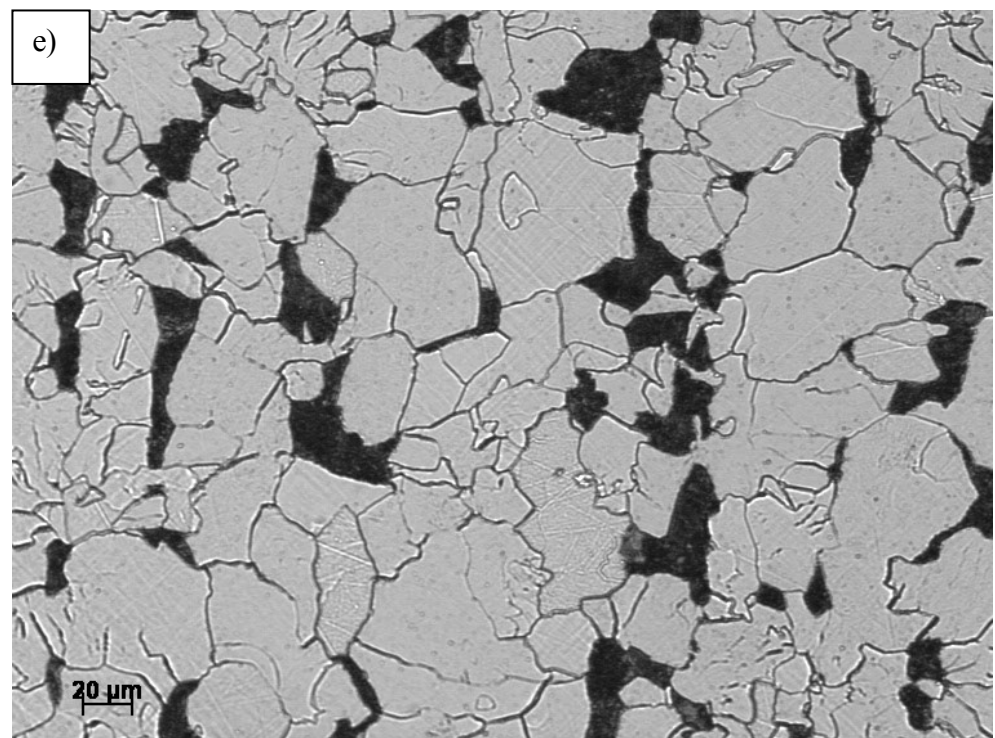
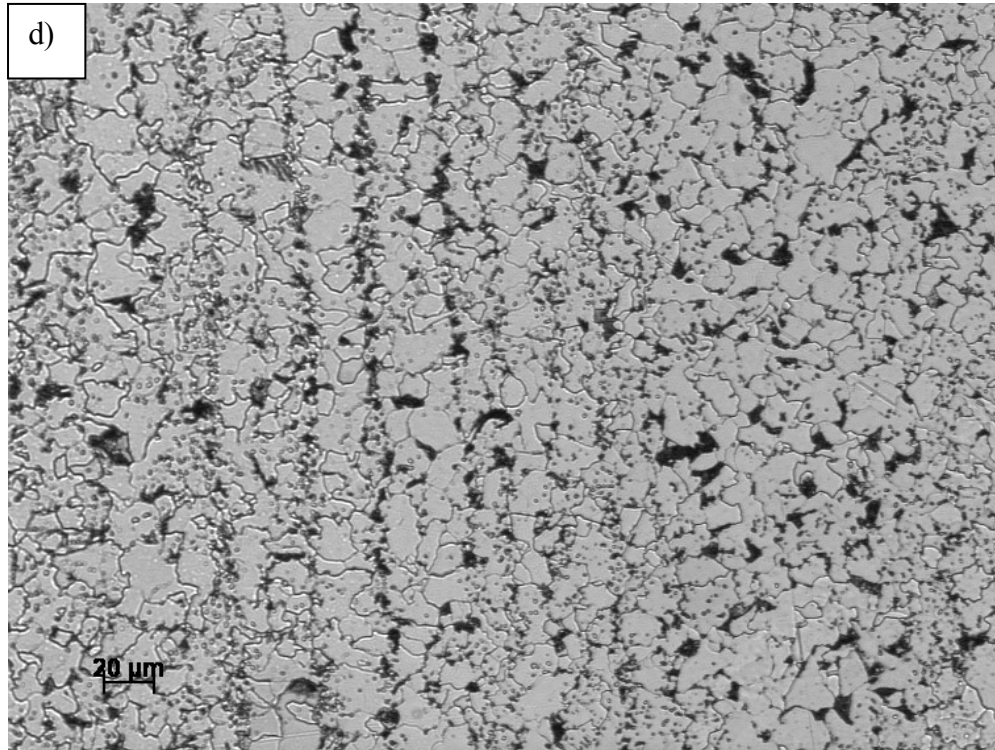
In S1-1100, S1-1200, S2-900 and S2-1100, most CIS were found to be related with cracked coarse TiN particles (therefore the crack was initiated from inside of the TiN particle, Figure 4.6 a)-f)), while there were still several (around 10% of the total CIS amount) cleavage fracture initiated at the edge of TiN particles, which was considered mainly due to the rectangular shape caused debonding initiation sites (Figure 4.6 g) and h)).

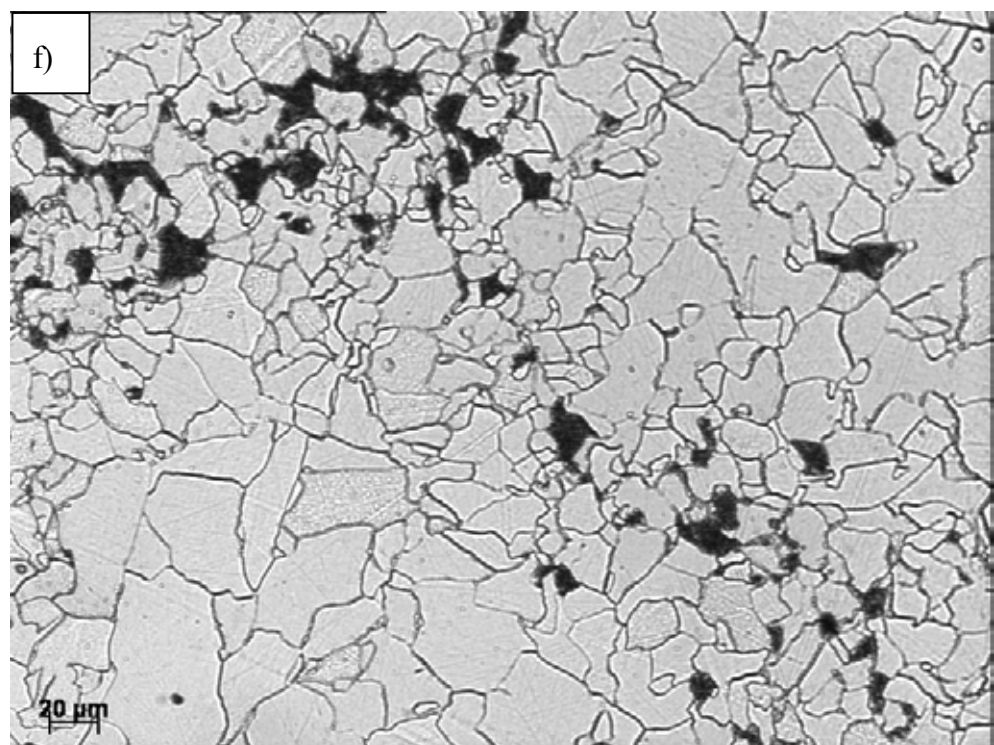
However, CIS or FIS could not be found easily in S1-900 samples due to the small grain size, and no identifiable features observed even a FIS or CIS was found, Figure 4.7 shows the typical fracture surface of this material.

In Steel 3, in which no coarse TiN particles are present, analysis of the fracture surfaces sometimes revealed a fracture initiation site, but no clear initiating features were observed (shown in Figure 4.8). This suggests that cracks are initiated from grain boundary carbides as these are present in the microstructure and are the most likely source of cleavage initiation.









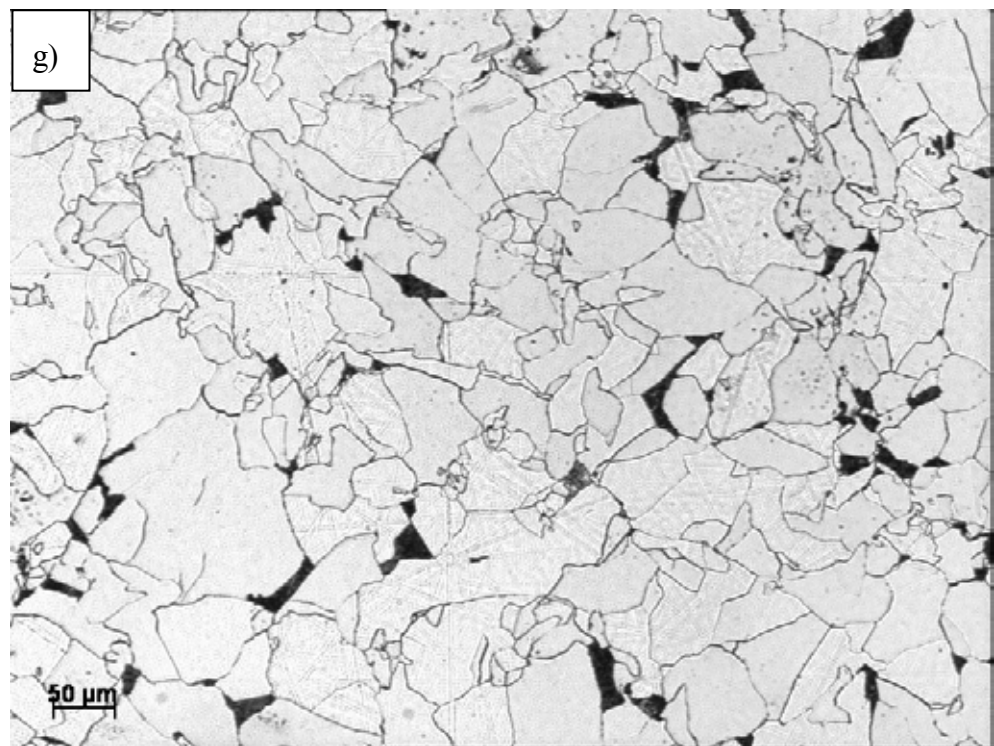


Figure 4.1-Optical micrograph showing the ferrite+pearlite microstructure with different grain sizes of investigated steels after austenitising at different temperatures for 30 minutes: a) S1-900, b) S1-1100, c) S1-1200, d) S2-900, e) S2-1100, f) S3-1100 and e) S3-1200.

## Chapter 4 - Results

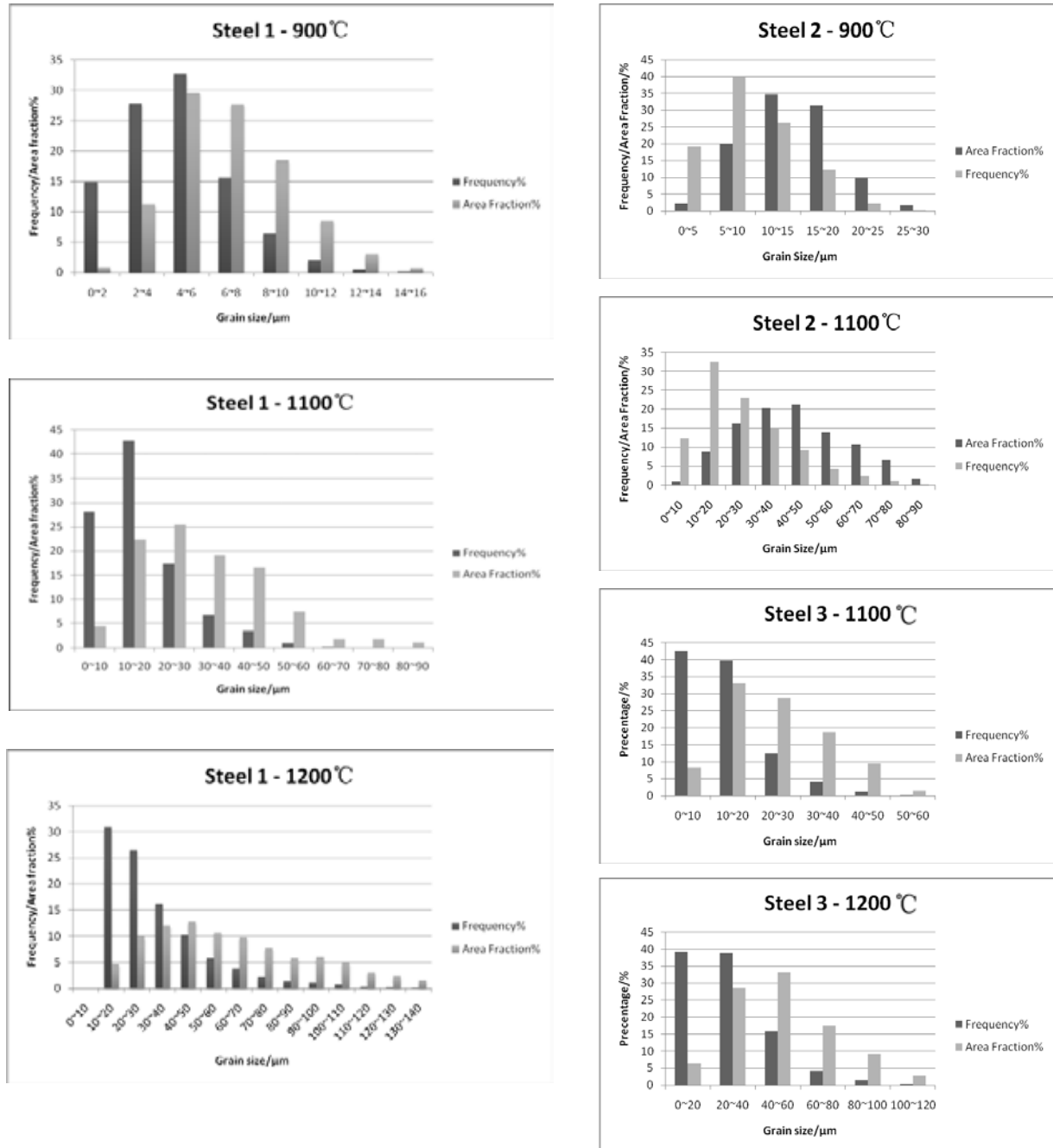


Figure 4.2-Grain size distributions (in number frequency and area fraction) of the materials after heat treatments.

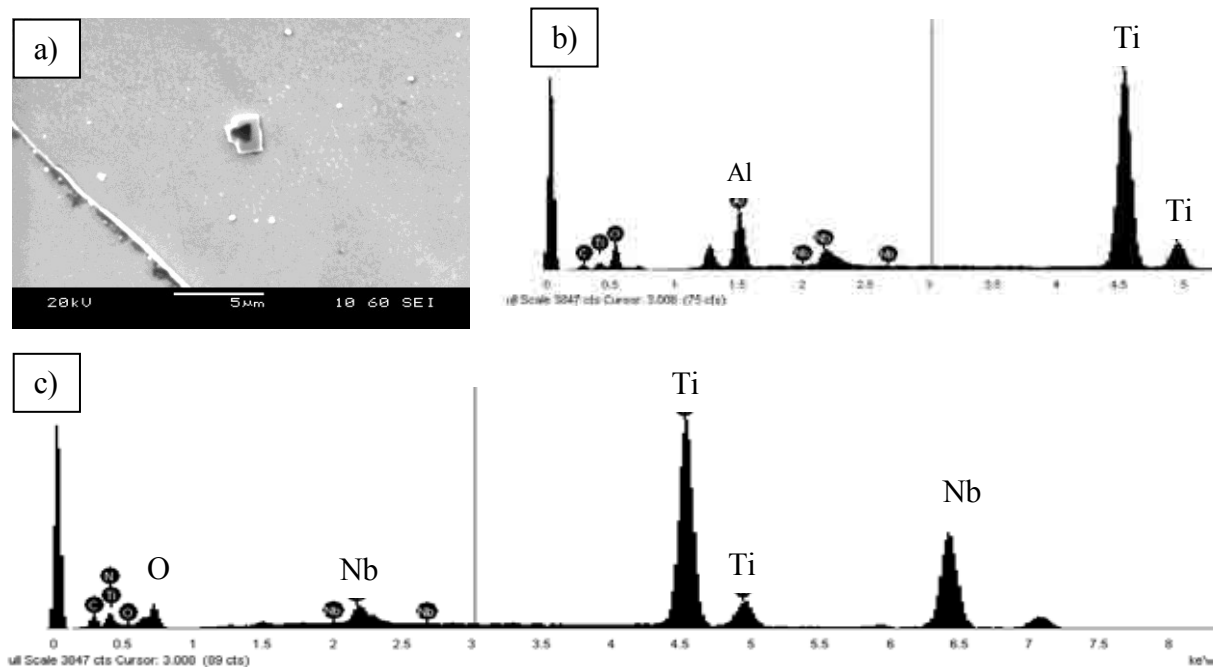


Figure 4.3-a) A typical TiN (grey) particle found in S1-1100 surrounding an  $\text{Al}_2\text{O}_3$  (black) inclusion, b) EDS result of the black centre of particle and c) EDS result of the particle away from the black centre, the Nb peak is likely to be from  $\text{Nb}(\text{C},\text{N})$  that precipitated on the TiN inclusion.

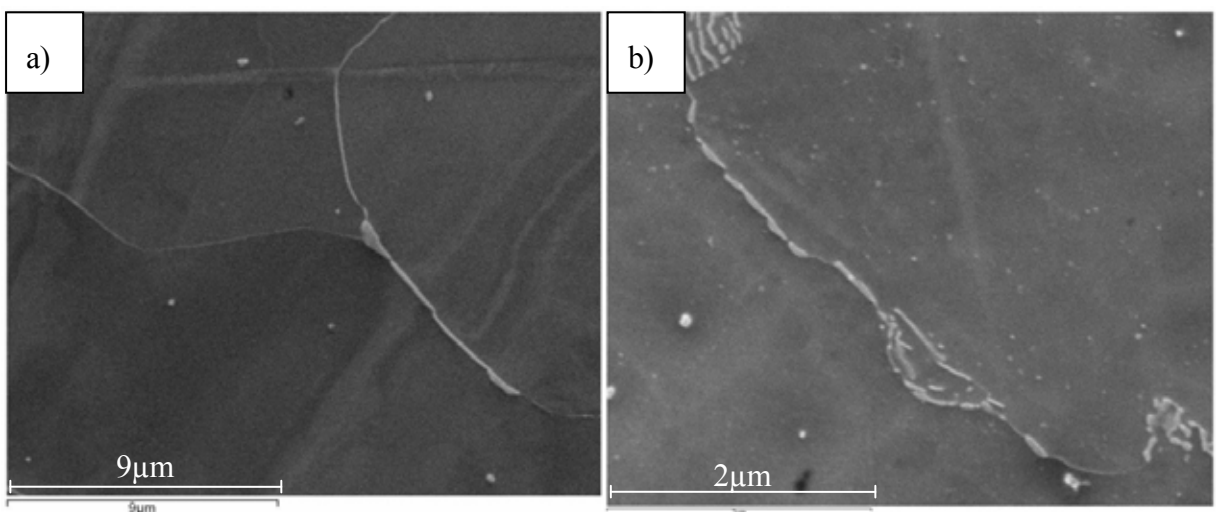
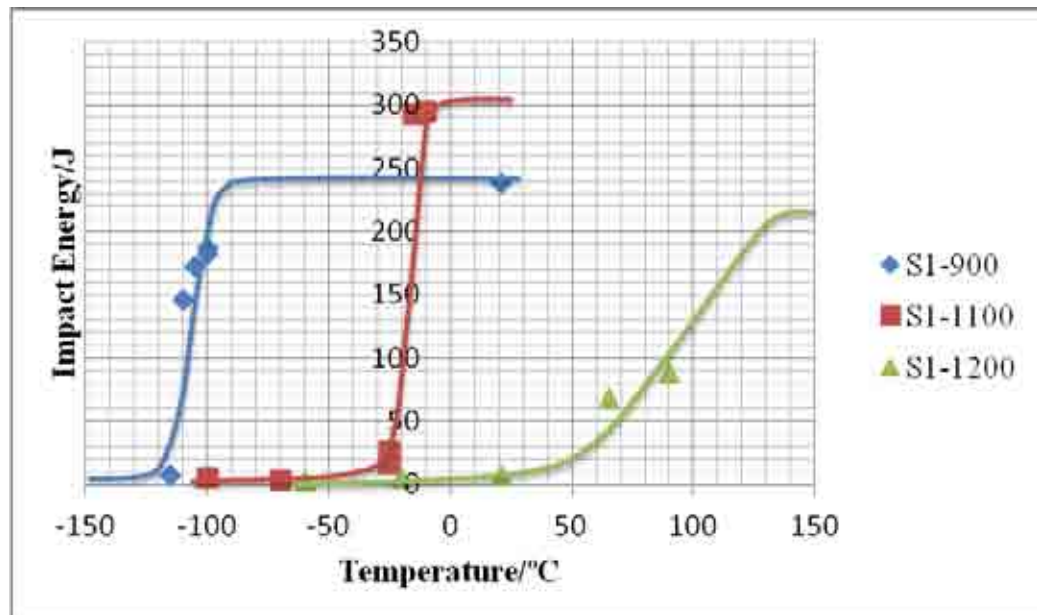
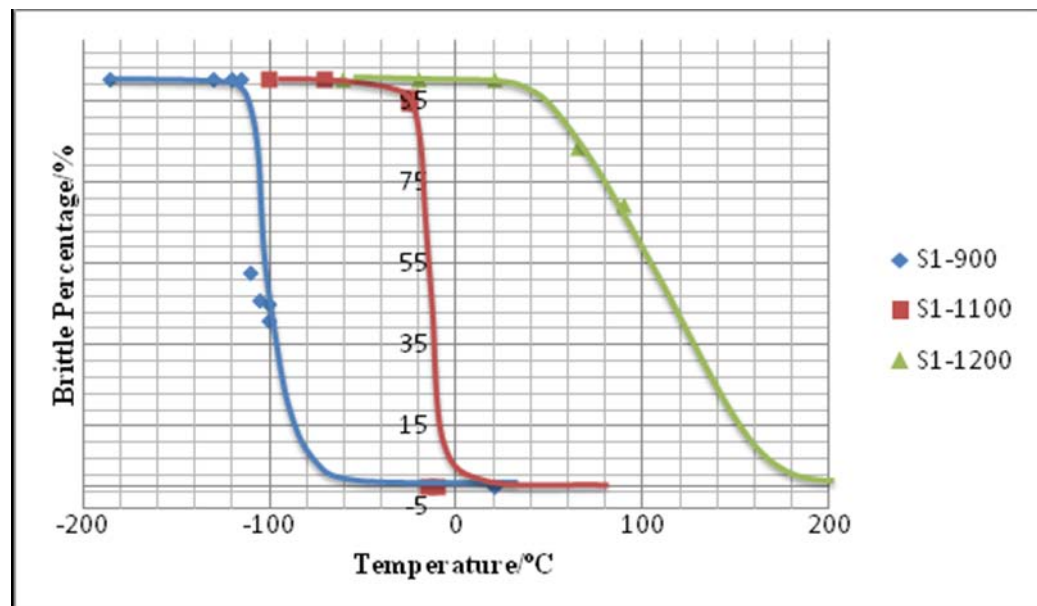


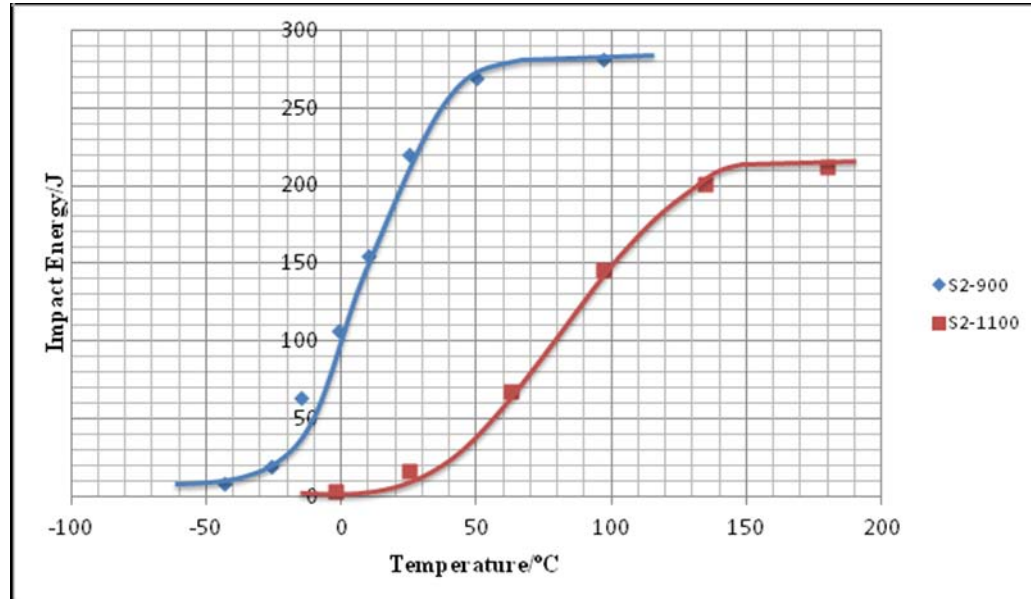
Figure 4.4-Grain boundary carbides found in the heat treated steels a) S1-1200 and b) S2-900.



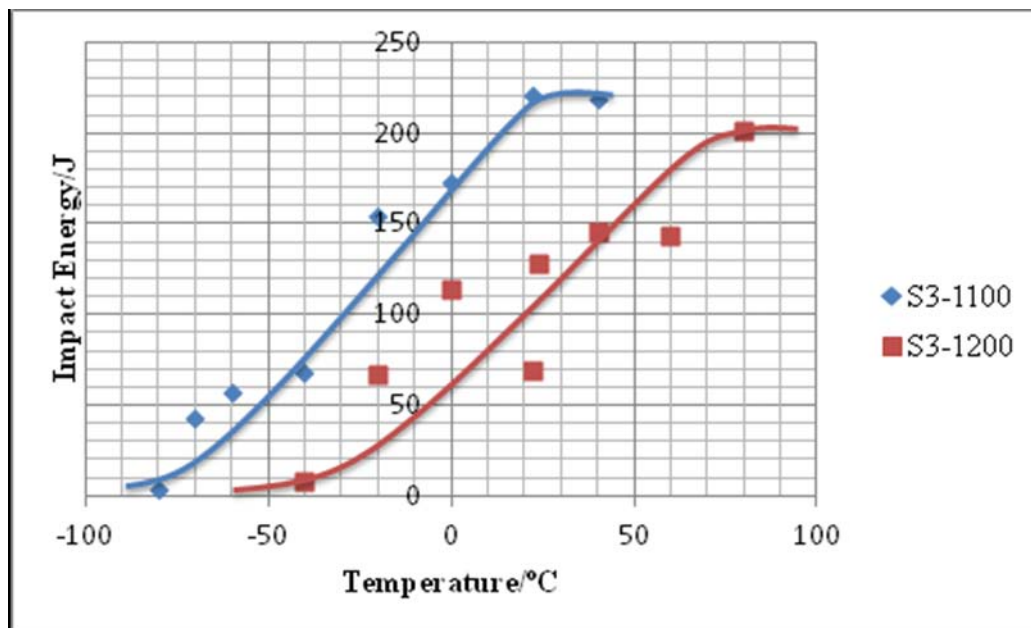
a)



b)

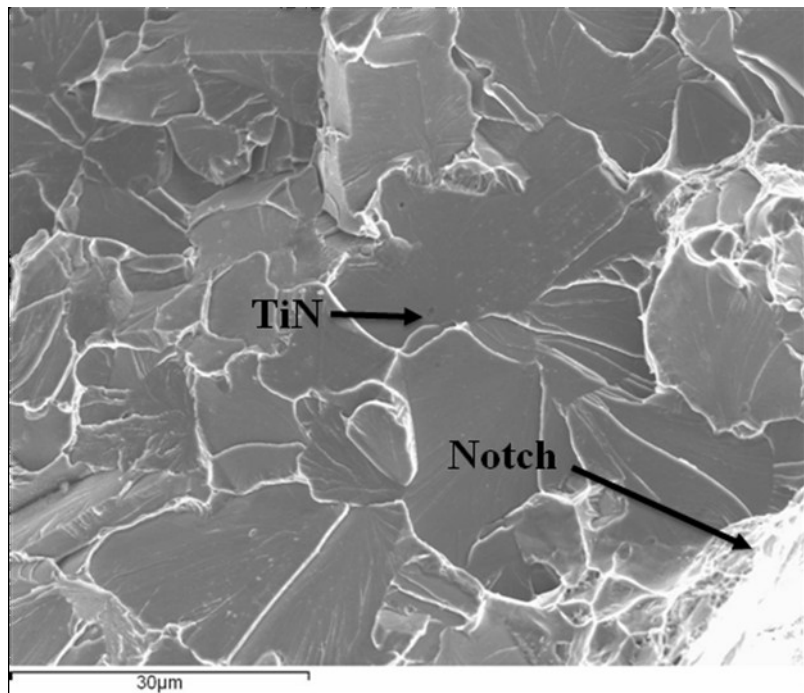


c)

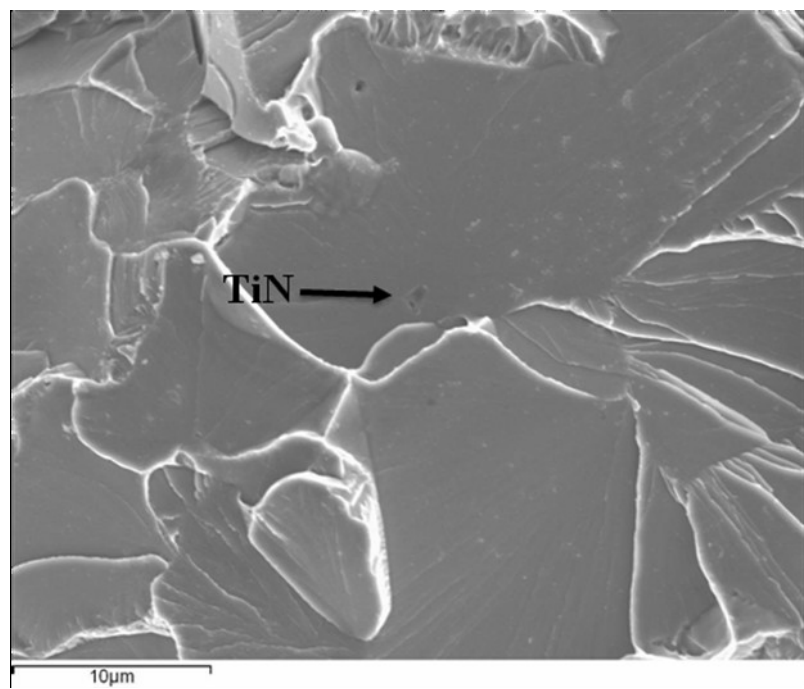


d)

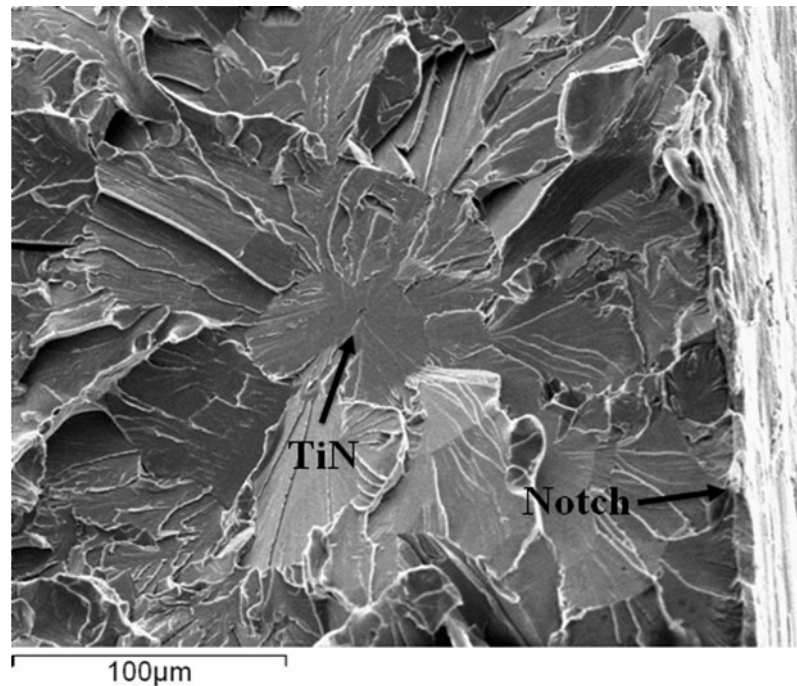
Figure 4.5-a) Impact energy transition curve of Steel 1 and b) fracture appearance transition curve of Steel 1, c) impact transition curve for Steel 2, d) impact transition curve of Steel 3.



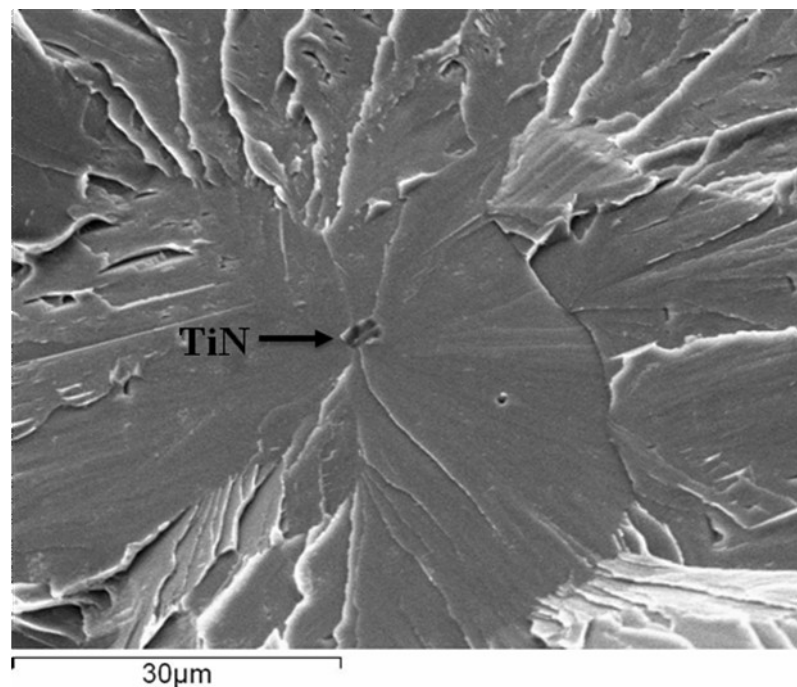
*a)*



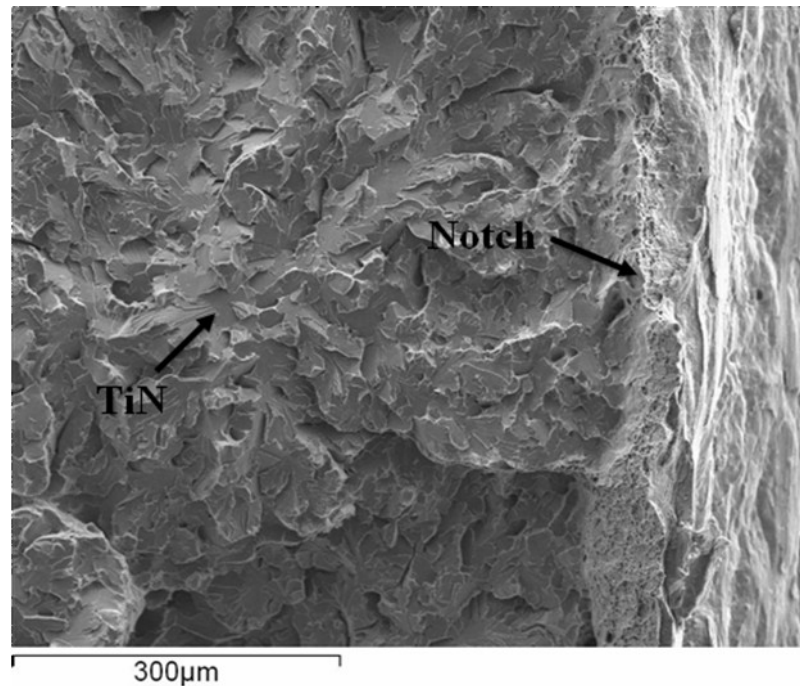
*b)*



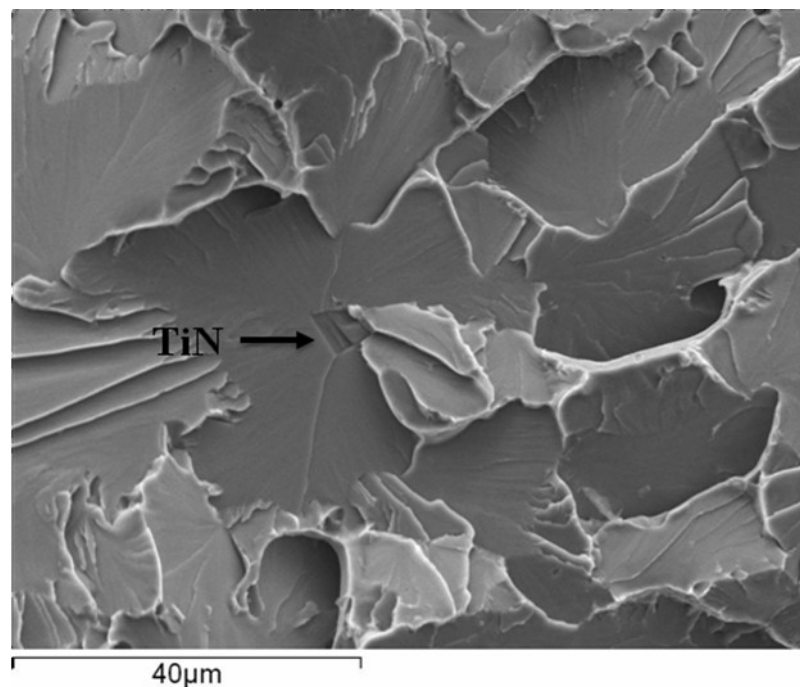
*c)*



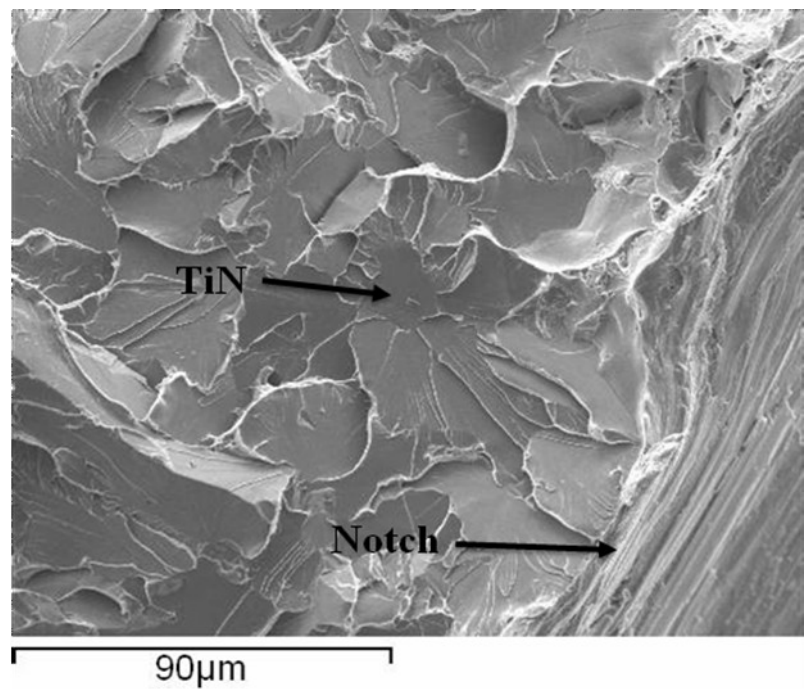
*d)*



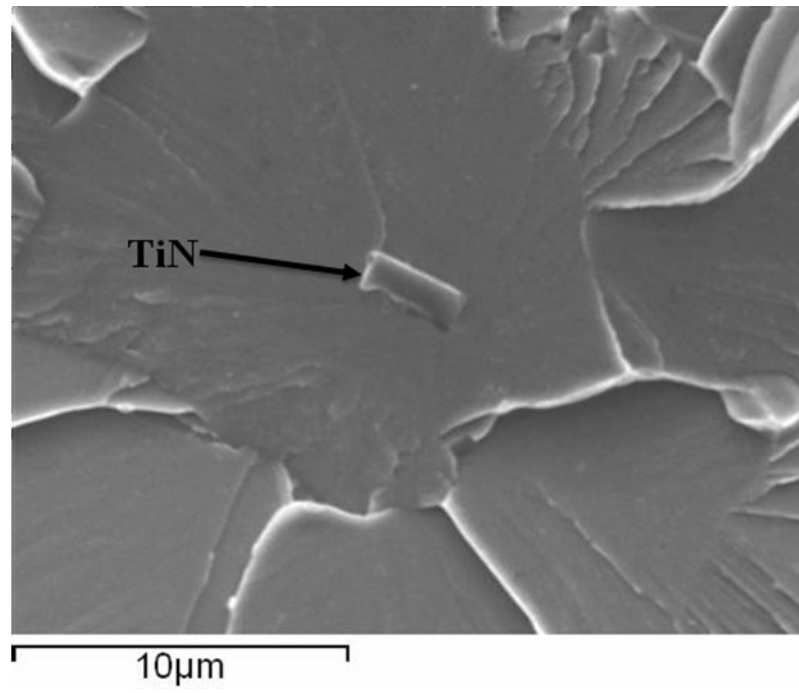
e)



f)



*g)*



h)

Figure 4.6- a), c), e) and g) SE images of coarse TiN particles found at initiation sites near notches in different heat treated specimens; b), d), f) and h) higher magnification image of the FIS of a), c), e) and g), respectively.

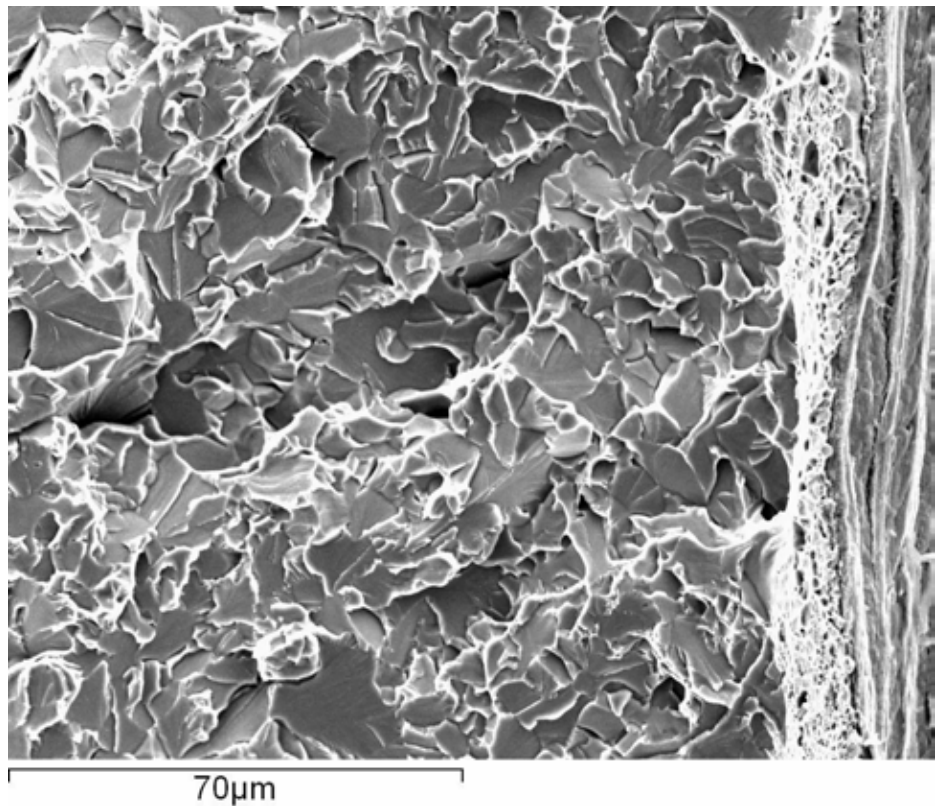


*Figure 4.7-Fracture surface of S1-900, no identifiable features considered as crack initiation sites could be observed*

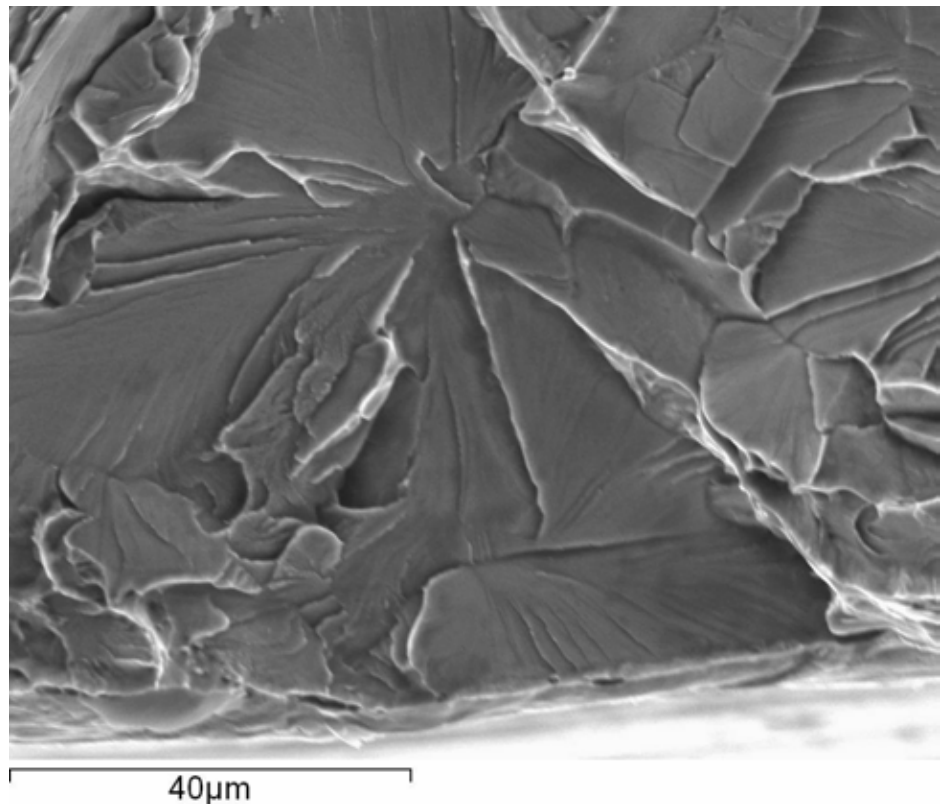


*Figure 4.8-A cleavage facet found in the S3-1100 specimen, no clear crack initiating feature was found, which suggests that the crack may have initiated from a grain boundary carbide.*

# **Chapter 5**

## **Discussion**

### **5.1 Crack Nucleation**

Micro-cracks can develop from hard particles and propagate depending on the conditions such as the crack length and the stress field around the crack tips. According to SEM fractography analysis, it has been found that TiN particles and grain boundary carbides are key factors of micro-crack nucleation in steels investigated, as shown in the results section, Figure 4.6 and Figure 4.8, respectively.

#### a). Grain boundary carbides

It is known that grain boundary carbides can play an important role in the fracture process as they can form a through thickness microcrack<sup>20,25,27,28</sup>. In this work, grain boundary carbides are taken into consideration by using the DBTT prediction equation by Mintz<sup>26,27</sup> (i.e. Eq.2.6) since they were found to act as crack initiators in tested specimens in all of the 3 steels (Figure 4.7 & 4.8).

#### b). TiN particles

In most low-carbon steels, TiN forms in the liquid state during solidification, and these particles can grow and coarsen very fast, especially in steels which have a high Ti content (where the Ti/N wt% ratio exceeds 3.42<sup>6</sup>).

As mentioned in section 2.8, TiN inclusions have often been found to act as a cleavage initiators in steels because they are brittle and can be present in statistically sufficient amounts. There is evidence in the literature indicating that debonding of a TiN inclusion from the matrix can act as the cleavage initiator<sup>33</sup>, which has also been found in this work (Figure 4.6 g), h)). Nevertheless, as

stated in the results section, in this work, the majority of observations showed that cleavage fracture was initiated by a cracked TiN particle (Figure 4.6 a)–f), crack within TiN particles can be seen clearly), rather than debonding of the inclusion from the matrix.

In some samples in the present research work, there are two other factors have been found that may influence microcrack initiation from a TiN particle, shown in Figure 5.1. One factor is the presence of a void former, such as MnS particles that have been observed connected with TiN particles; the other one is that a crack formed in the TiN particle itself. It can be seen in Figure 5.1 b) that the microcrack initiated inside the TiN particle may also be linked to the “black centre” of the TiN particle which has been assessed by EDS to be an  $\text{Al}_2\text{O}_3$  inclusion. Alumina is harder and have larger coefficient of thermal expansion compared with TiN<sup>24</sup>, and therefore its presence can be regarded as a large internal defect in the TiN particle. It can be seen from the arrow in Figure 5.1 b) that the microcrack may have formed inside the TiN particle from a sharp corner of the  $\text{Al}_2\text{O}_3$  inclusion.

Therefore, microcracks can form not in the matrix from the TiN particles due to their characteristics of brittle and cubic in shape, but also inside the particles when an  $\text{Al}_2\text{O}_3$  inclusion exists in the TiN particle. Thus, TiN particles can be a strong initiator of cracks in steels especially when the tessellated stresses are taken into consideration, as described in the literature review.

However, even though a microcrack has formed in the TiN particle, whether it will penetrate the matrix or not depends on the level of the stress value (whether it exceeds the particle-matrix interface strength or not). The particle-matrix interface strength can be calculated by using the following equation:

$$\sigma_{pm} = \left( \frac{\pi E \gamma_{pm}}{(1-\nu^2)a} \right)^{1/2} \quad \text{Eq.5.1}$$

where E is the Young's modulus which can be generally taken as 220 GPa for steels, v is Poisson ratio which is generally 0.3 for steels,  $\gamma_{pm}$  is the particle-matrix interface energy and a is the size of particle. According to the previous research <sup>5</sup>, a value of 7 J/m<sup>2</sup> as an upper limit of  $\gamma_{pm}$  has been defined, and this value does not change much as the temperature increases. This indicates that once the loading stress value exceeds the particle-matrix strength  $\sigma_{pm}$ , then the microcrack will penetrate the matrix immediately, which means the cleavage fracture will happen at this level of loading (shown in Figure 4.6 c), d)).

Figure 5.2 shows a grain-sized crack arrested at a grain boundary due to insufficient stress found in S2-1100, which was also observed in specimens S1-1100, S1-1200 and S2-900, all of which have coarse TiN particles and large grain size (above 9.5μm), however, whether TiN particles initiated these cracks or not is unclear due to the 2D section view meaning that the probability of observing a TiN particle is small. It can be seen from Figure 5.2 that the angle ( $\beta$ ) between the loading direction, which is parallel to the Charpy specimen length direction (shown on the figure), and the cleavage facet, i.e. the crack plane, is small, which means the actual fracture stress on the facet ( $\sigma_{F-act}$ ) is much less than the overall calculated value ( $\sigma_{F-calc}$ ):

$$\sigma_{F-act} = \sigma_{F-calc} \cos \beta \quad \text{Eq.5.2}$$

The possibility of propagation of a grain-sized crack depends on the matrix strength, which can be calculated from the equation below (an assumption that the fracture stress  $\sigma_{mm}$  is perpendicular to the first facet has been made in the calculation):

$$\sigma_{mm} = \left( \frac{\pi E \gamma_{mm}}{(1-\nu^2)D} \right)^{1/2} \quad \text{Eq.5.3}$$

where  $\gamma_{mm}$  is the effective surface energy for fracture at the matrix-matrix interface, and D is the average grain size. According to the previous research, the surface energy  $\gamma_{mm}$  changes significantly with temperature<sup>22,25</sup>, from 50 J/m<sup>2</sup> at 77 K to 500 J/m<sup>2</sup> at 223 K.

## 5.2 Combination of the Effect of Particles and Grain Size

For Steel 1 and Steel 2, since cracks will have already nucleated from coarse TiN particles (evidenced by the fracture surface analysis shown in Figure 4.6 b), d) and e)), which is the first step in the fracture process, the second step, crack propagation from particles into the matrix, and the third step, crack propagation across matrix grain boundaries, become very important in the cleavage fracture process. According to the discussion in section 2.6, whether crack propagation is particle controlled or grain size controlled can be determined by comparing the two critical stress values:  $\sigma_{pm}$  and  $\sigma_{mm}$ , (from equations 5.1 and 5.3) shown in Table 5.1, where D is average grain size, a is average particle size,  $D_{crit}$  is the calculated critical grain size when the  $\sigma_{mm}$  equals to  $\sigma_{pm}$ .

Table 5.1. Comparison of  $\sigma_{pm}$  and  $\sigma_{mm}$  values of three steels

	Heat treated temperature/°C	D/μm	$\sigma_{mm}$ /MPa	a/μm	TiN No. density/mm <sup>-1</sup>	$\sigma_{pm}$ /MPa	$D_{crit}$ /μm
Steel 1	900	4.6	2873	1.62	88	1812	11.57
	1100	13.2	1696				
	1200	27.3	1179				
Steel 2	900	9.5	1999	3.47	14	1238	24.78
	1100	25.4	1223				
Steel 3	1100	13.5	1677	-	-	-	-
	1200	28.4	1156				

In order to investigate the cleavage fracture behaviour of each steel at low temperatures when calculating the  $\sigma_{pm}$  and  $\sigma_{mm}$  values, the surface energies  $\gamma_{pm}$  and  $\gamma_{mm}$  at 77 K were taken as 7 J/mm<sup>2</sup> and 50 J/mm<sup>2</sup>, respectively<sup>5</sup>, it can be seen from Table 5.1 that  $\sigma_{mm}$  values always decrease with the increase of heat treatment temperature (associated with the increase in ferrite grain size), while  $\sigma_{pm}$  values stay the same due to the fact that the average particle (TiN) sizes do not change with the heat treatment temperature.

For cracks initiated from grain boundary carbides, it is also necessary to take the fracture stress of the carbides into consideration. It has been reported that the surface energy of grain boundary carbides is around 9 J/m<sup>2</sup><sup>27</sup> which is slightly higher than TiN, then the fracture stresses to crack carbides are calculated to be from 3923 MPa ( $t=0.18 \mu\text{m}$ ) to 6290 MPa ( $t=0.07 \mu\text{m}$ ) according to the relevant equation<sup>27</sup>, which is higher than the fracture stress of TiN particles and this illustrates that TiN particles should fracture before grain boundary carbides.

Therefore, by comparing the  $\sigma_{pm}$  and  $\sigma_{mm}$  values shown in Table 5.1, it can be seen that for Steel 1, only the  $\sigma_{mm}$  of S1-900 is higher than  $\sigma_{pm}$ , and for Steel 2 only S2-900 is higher than  $\sigma_{pm}$ , therefore, it is expected that the S1-900 and S2-900 are grain size controlled cleavage fracture while S1-1100, S1-1200 and S2-1100 are particle controlled fracture according to pure fracture stress analysis.

However, when the temperature increases, the surface energy of ferrite ( $\gamma_{mm}$ ) will increase accordingly, but this trend depends on chemical composition and there are few data available at present on the exact variation in surface energy; previous research has shown variable results<sup>5,22</sup>.

Therefore the critical grain size ( $D_{crit}$ ) value will vary as the surface energy increases significantly with temperature and therefore cannot be readily used to predict where fracture will be grain size or particle controlled at temperatures above approx -196 °C, i.e. corresponding to the DBTT seen in this work. For example, the surface energy of ferrite is reported to be around 500 J/m<sup>2</sup> at -50 °C<sup>5</sup>, and then the calculated  $D_{crit}$  will be 116  $\mu\text{m}$  for Steel 1 and 248  $\mu\text{m}$  for Steel 2, which means that

for all the heat treated samples, as the actual grains are smaller than this value, the fracture should be grain size-controlled, i.e. the crack formed by a TiN particle should not propagate to failure. However, by investigating the fracture surfaces, the failures of S1-1100, S1-1200, S2-900 and S2-1100 in the lower transition temperature range are suggested to be particle-controlled since overall fracture initiation sites from TiN particles were observed.

### **5.3 Relationship between TiN particles, grain size and impact toughness**

For Steel 3, which contains no coarse TiN particles, there is a consistent difference (around 30 °C) between the predicted and measured DBTT. This is likely to be due to inaccuracies in the DBTT prediction by the Mintz equation. It should be noted that Steel 3 contains a small amount, 0.5 wt%, of Ni, which is known to improve toughness<sup>32</sup>, and Ni is not accounted for in the Mintz equation. Therefore, by including an effect of Ni on the DBTT prediction, which will be consistent for the two heat treatment conditions, the effect of grain size changes can be accounted for by the Mintz equation (grain size increase from 16 µm to 28 µm results in the increase of both actual and predicted DBTT of about 55 °C).

The composition of Steel 2 is in the range for which the Mintz equation is valid and it can be seen from Table 7 that the DBTT of S2-1100 sample (grain size of 25.4 µm) is very well predicted, however, the predicted DBTT value of S2-900, which has a grain size of 9.5 µm, is 16 °C lower than the experimental value. Some experimental variability and scatter is expected during Charpy impact testing, and the fact that TiN particles were seen as fracture initiation sites for both steels, suggests that the difference of  $\Delta$ DBTT = 16 °C is due to experimental scatter. This suggests that the Mintz equation is predicting the DBTT values satisfactorily and that, whilst the TiN particles can initiate cleavage, the effect of coarse TiN particles being present in this steel on the DBTT is

small, which means the fracture is controlled by grain boundary carbides, as announced in the Mintz equation.

Considering Steel 1 it can be seen that for the 5  $\mu\text{m}$  and 27.4  $\mu\text{m}$  grain size samples (S1-900 and S1-1200) the predicted and experimental DBTT values are very close ( $\Delta\text{DBTT}$  of 2 and 5  $^{\circ}\text{C}$  respectively). For the S1-900 samples no TiN initiated fracture was observed, whilst for the S1-1200 samples TiN initiated fracture was observed. This suggests that the Mintz equation is able to predict the DBTT satisfactorily and that the coarse TiN particles do not have a significant effect on the DBTT. There is a difference between the predicted and experimental DBTT values for the S1-1100 samples (grain size of 13  $\mu\text{m}$ ,  $\Delta\text{DBTT}$  of 22  $^{\circ}\text{C}$ ), it is suggested that this discrepancy is due to experimental scatter as the experimental DBTT is lower, i.e. better toughness, than the predicted value, which indicates that TiN is not having a significant influence on the toughness properties.

In summary, for Steels 1 and 2, there is acceptable agreement between the predicted and measured DBTT values for all samples, indicating that the effect of TiN inclusions on toughness is not significant and the Mintz equation can be used successfully. The reason for this is that the TiN particles may have an effect on crack initiation but at the Charpy impact test temperatures the matrix-matrix interface energy will be higher than that used to predict the critical grain sizes in Table 8, giving a much larger critical grain size, and therefore crack propagation is more strongly influenced by the ferrite grain size.

Besides, the strength (or softness) of material, which may be affected by alloy elements, will also have an effect on crack propagation. It has been proved by previous research work<sup>34</sup> that a matrix with a lower strength indicates a better impact toughness due to the reduced matrix strength lessened transferred stress levels.

Moreover, the testing methods also have effects on the experimental results. In impact testing, energy are used in both crack nucleation and propagation, while in bending tests (or CTOD tests), the energy are mainly used in crack nucleation.

Therefore, it may be speculated that the TiN particles may have an effect on the fracture stress, for example measured by blunt notch testing at low temperatures, around -196°C, where the critical grain size calculation is valid as the matrix-matrix interface energy is known.

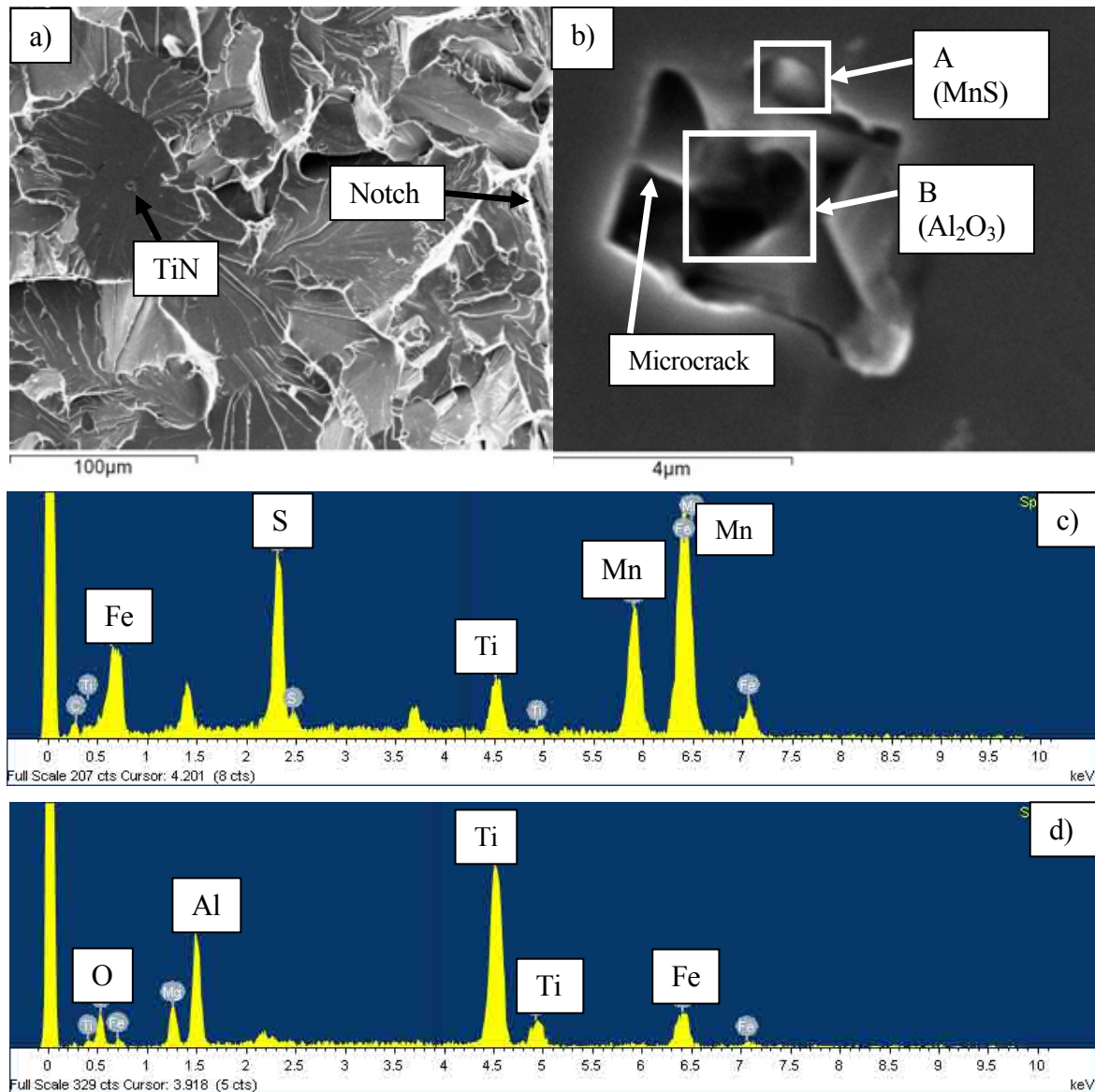


Figure 5.1-MnS and Al<sub>2</sub>O<sub>3</sub> inclusions in/on a TiN particle which initiated final failure of SI-1200.

a) Fracture surface, it can be seen that a TiN particle is acting as the fracture initiation site by tracing the “river pattern”; b) A higher magnification image of the TiN particle; c) EDS result for point A in image b), showing that point A is a MnS inclusion; d) EDS result for point B in graph b), the “black centre” of the TiN particle shown to be a Al<sub>2</sub>O<sub>3</sub> inclusion.

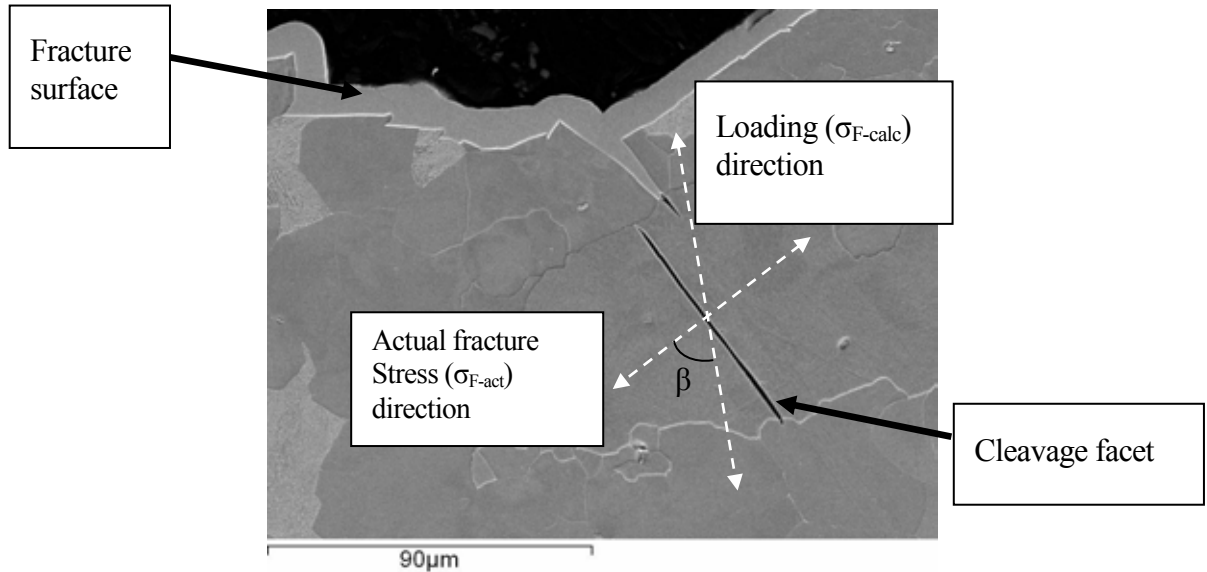


Figure 5.2-A grain-sized crack arrested at a grain boundary beneath the fracture surface of S2-1100.

1100.

# **Chapter 6**

## **Conclusions and Future Work**

### **6.1 Conclusions**

The Charpy impact DBTT has been predicted and experimentally determined for three low carbon steels heat treated to give different ferrite grain sizes. The effect of the presence of coarse ( $> 0.5 \mu\text{m}$ ) TiN particles on the DBTT has been assessed.

1. In the absence of coarse TiN particles the effect of changes in ferrite grain size was predicted well by the Mintz equation, although there was a significant effect attributed to Ni (present as 0.50 wt% in the steel not containing TiN particles) on the DBTT values.
2. When coarse TiN particles were present in the steels then they were observed to cause cleavage fracture initiation sites for the heat treated samples with average ferrite grain sizes in the range  $9.5 - 27.3 \mu\text{m}$ , however for the sample with an average grain size of  $5.0 \mu\text{m}$  no TiN initiated cleavage was observed.
3. Despite the observation of cleavage initiation from TiN particles it was found that there was no significant effect of the coarse TiN particles on the Charpy impact DBTT with the DBTT values being adequately predicted by the Mintz equation across the ferrite grain size range from  $5 - 27.3 \mu\text{m}$ .
4. Fracture stress analysis, for example to calculate a critical ferrite grain size above which fracture is predicted to be particle controlled, cannot be used readily to determine if TiN particles will affect the Charpy impact behaviour as the ferrite interface energy,  $\gamma$ , changes significantly with temperature and this relationship is not yet fully quantified.

## **6.2 Suggestions for future work**

1. This research work focused on low carbon ferritic steels only, however, some other microstructures such as bainite and martensite could appear instead of ferrite and pearlite when using other heat treatment routes. It is known that for steels with the same grain size, matrix hardening or strengthening will decrease toughness <sup>1,9,19,21</sup>. Therefore it could be useful to investigate the effect of TiN particles in bainitic and martensitic steels.
2. The effect of Ni on the toughness (in particular Charpy impact toughness) in steels also needed to be investigated in more detail to provide more quantitative data as many more modern steels contain small Ni additions.
3. The fracture stress analysis cannot be applied easily in this work due to the significant increase of ferrite matrix surface energy at higher temperature, but it is still relevant to study the fracture behaviour of steels containing TiN particles by doing bending tests at low temperatures (for example liquid nitrogen temperature) since the surface energies are already known or easy to estimate.

## References

- 1 Comstock, G. F. *Titanium in Iron and Steel.* 30-47, 48-55, 95-128, 129-163, 231-261 (John Wiley & Sons, Inc, 1955).
- 2 Linaza, M. A., Romero, J. L., Rodriguez-Ibane, J. M. & Urcola, J. J. Influence of the microstructure on the fracture toughness and fracture mechanisms of forging steels microalloyed with titanium with ferrite-pearlite structures. *Scripta Metallurgica et Materialia* **29**, 451-456 (1993).
- 3 Linaza, M. A., Romero, J. L., Rodriguez-Ibane, J. M. & Urcola, J. J. Cleavage fracture of microalloyed forging steels. *Scripta Metallurgica et Materialia* **32**, 395-400 (1995).
- 4 Fairchild, D. P., Howden, D. G. & Clark, W. A. T. The mechanism of brittle fracture in a microalloyed steel: Part I. Inclusion Induced Cleavage. *Metall Mater Trans A* **31A**, 641-652 (2000).
- 5 Martin, J. I. S. & Rodriguez-Ibane, J. M. Determination of energetic parameters controlling cleavage fracture in a Ti-V microalloyed ferrite-pearlite steel. *Scripta Materialia* **40**, 459-464 (1999).
- 6 Yan, W., Shan, Y. Y. & Yang, K. Effect of TiN inclusions on the impact toughness of low-carbon microalloyed steels. *Metall Mater Trans A* **37A**, 2147-2158 (2006).
- 7 Zhang, L. P., Davis, C. L. & Strangwood, M. Dependency of fracture toughness on the inhomogeneity of coarse TiN particle distribution in a low alloy steel. *Metall Mater Trans A* **32A**, 1147-1155 (2001).
- 8 Zhang, L. P. *Microstructure and Fracture Toughness in the HAZ of a Structural Steel Containing TiN Particles* PhD thesis, The University of Birmingham, (2000).
- 9 Aaronson, B. *Steel Strengthening Mechanisms.* (Climax Molybdenum Co., 1969).
- 10 Bhadeshia, H. K. D. H. & Honeycombe, R. W. K. *Steels: microstructure and properties.* 3rd ed. edn, 40, 71-92 (Elsevier Ltd., 2006).
- 11 Schneider, S. J. *Engineering Materials Handbook (4): Ceramics and Glasses.* (ASM International, 1991).
- 12 Xu, G. K. & Chen, J. J. *V-Ti Casting Iron and Steel.* in Chinese edn, 6 (Metallurgy Industry Ltd, 1995).
- 13 Ringer, S. P., R.P.Kuziak & Easterling, E. K. Liquid film simulation of Zener grain boundary pinning by second phase particles. *Mater Sci Tech-Lond* **7**, 193-200 (1991).
- 14 Li, W. B. & Easterling, E. K. The influence of particle shape on zener drag. *Acta Metallurgica et Materialia* **38**, 1045-1052 (1990).
- 15 Ringer, S. P., Li, W. B. & Easterling, E. K. On the interaction and pinning of grain boundaries by cubic shaped precipitate particles. *Acta Metallurgica* **37**, 831-841 (1989).
- 16 Narita, K. *Trans. Iron and Steel Inst. of Japan.* Vol. 15 145 (1975).
- 17 Mintz, B. Hot Ductility of Steel. (City University, London, 1998).
- 18 Wang, S. C. The effect of titanium and nitrogen contents on the austenite grain coarsening temperature. *J Mater Sci* **24** (1989).
- 19 Yu, Y. N. *Foundamental of Materials Science.* 571-573, 629 (Higher Education Press, 2006).
- 20 Petch, N. J. The Influence of Grain Boundary Carbide and Grain Size on the Cleavege Strength and Impact Transition Temperature of Steel. *Acta Metall* **34**, 1387-1393 (1986).

## References

- 21 Yang, W. Y. & Qiang, W. J. *Mechanical Behavior of Materials.* 76-105 (Chemical Industry Press, 2009).
- 22 Linaza, M. A., Rodriguez-Ibane, J. M. & Urcola, J. J. Determination of the energetic parameters controlling cleavage fracture initiation in steels. *Fatigue Fract. Engng Mater. Struct.* **20**, 619-632 (1997).
- 23 Fairchild, D. P., Howden, D. G. & Clark, W. A. T. The mechanism of brittle fracture in a microalloyed steel: Part II. Mechanic Modeling. *Metall Mater Trans A* **31A**, 653-667 (2000).
- 24 Yan, W., Shan, Y. Y. & Yang, K. Influence of TiN Inclusions on the Cleavage Fracture Behavior of Low-Carbon Microalloyed Steels. *Metallurgical and Materials Transactions A* **38**, 1211-1222, doi:10.1007/s11661-007-9161-2 (2007).
- 25 Lin, T., Evans, A. G. & Richie, R. O. Stochastic Modeling of the Independent Roles of Particle Size and Grain Size in Transgranular Cleavage Fracture. *Metallurgical Transactions A* **18A**, 641-651 (1987).
- 26 Bhattacharjee, D., Knott, J. F. & Davis, C. L. Charpy-Impact-Toughness Prediction using an “Effective” Grain Size for Thermomechanically Controlled Rolled Microalloyed Steels. *Metall Mater Trans A* **35A**, 121-130 (2004).
- 27 Mintz, B., Morrison, W. B. & Cochrane, R. C. in *Advances in the physical metallurgy and applications of steels.* (The Matels Society).
- 28 Mintz, B., Morrison, W. B. & Jones, A. Influence of carbide thickness on transition temperature of ferritic steels. *Met Technol* **6**, 252-260 (1979).
- 29 Wu, S. J. *Micro-mechanisms of Fracture in Transition Welds* PhD thesis, The University of Birmingham, (1997).
- 30 Pavlina, E. J. & Tyne, C. J. V. Correlation of Yield Strength and Tensile Strength with Hardness for Steels. *Materials Engineering and Performance* **17**, 888-893 (2008).
- 31 International, A. (100 Barr Harbor Drive, PO Box C-700, West Conshohocken, Pennsylvania 19428-2959, United States, 2007).
- 32 Krawczyk, J., BaŁA, P. & Pacyna, J. The effect of carbide precipitate morphology on fracture toughness in low-tempered steels containing Ni. *Journal of Microscopy* **237**, 411-415, doi:10.1111/j.1365-2818.2009.03275.x (2010).
- 33 Harrison, P. L. & Bateson, P. H. *Proc. Conf. Titanium Technology in Microalloyed Steels.* 180-196 (T.N. Baker, 1994).
- 34 Balart, M. J., Davis, C. L. & Strangwood, M. Cleavage initiation in Ti-V-N and V-N microalloyed ferritic-pearlitic forging steels. *Materials Science and Engineering A* **284**, 1-13 (2000).